AIMS Materials Science, 5(4): 650–698.
DOI: 10.3934/matersci.2018.4.650
Received: 10 July 2018
Accepted: 07 August 2018
Published: 14 August 2018

http://www.aimspress.com/journal/Materials

Review

In situ Raman analyses of electrode materials for Li-ion batteries

Christian M. Julien* and Alain Mauger

Sorbonne Université, Campus Pierre et Marie Curie, Institut de Minéralogie, Physique des Matériaux et de Cosmochimie (IMPMC), UMR 7590, 4 place Jussieu, 75005 Paris, France

*** Correspondence:** Email: christian.julien@upmc.fr.

Abstract: The purpose of this review is to acknowledge the current state-of-the-art and the progress of *in situ* Raman spectro-electrochemistry, which has been made on all the elements in lithium-ion batteries: positive (cathode) and negative (anode) electrode materials. This technique allows the studies of structural change at the short-range scale, the electrode degradation and the formation of solid electrolyte interphase (SEI) layer. We also discuss the results in the perspective of spatial and real-time investigations by *in situ* Raman imaging (mapping) during charge/discharge cycling.

Keywords: *in situ* Raman spectro-electrochemistry; lithium-ion batteries; electrode materials

1. Introduction

The improvement of high performance lithium-ion batteries requires an optimization of the structure of materials, the knowledge of the mechanism of the intercalation/deintercalation of Li^+ into/from host materials as well as the kinetics of the electrolytic reaction [1]. Since the early report by Novák et al. [2], only few articles have addressed an overview of *in situ* microscopic studies on the structural and chemical behaviors of lithium-ion battery materials [3–5]. In this respect, in operando or *in situ* analytical techniques have been widely developed to investigate dynamic systems such as material growth [6], insertion/deinsertion reaction [7], phase stability [8], interface evolution [9], compatibility between materials [10], electrode degradation [11,12], etc.

As a non-destructive and sensitive method, Raman spectroscopy (RS) is a powerful analytical technique that has the potential to study electrode materials under *in situ* conditions. RS involves an inelastic scattering of the electromagnetic radiation by the matter, characterized by a shift of the frequency of the scattered light with respect to the incident light. This shift is equal to the frequency of the vibrational modes of atoms or molecules that are Raman active, which depends only on their

symmetry. Consequently, RS is a primary tool used to probe the structural evolution and the chemical composition of materials composing a lithium-ion battery. It gives information on the local structure (short-range order), in contrast to X-ray diffraction (XRD) that probes the long-range order of the matter. Therefore, RS is a complementary tool to diffraction techniques (X-ray, electron, neutron) to investigate the local structure of transition-metal oxides used as positive electrodes in lithium-ion batteries [13]. It proved to be very useful in characterizing the phase transformations in such materials upon cycling [14] or heat treatment [15]. Such changes can affect only the surface of the particles, in which case they are not detected by diffraction techniques. RS is also a powerful analytical technique for the knowledge of the structure of either disordered or amorphous compounds [16,17]. It should be noted that, in general, non-stoichiometry, substitutions or ion exchanges in a non-ideal material are violating the selection rules giving rise to additional bands, wavenumber shifts and/or band broadenings. For instance, Raman spectroscopy was employed to probe the nucleation and growth and structure of pulsed-laser deposited (PLD) V_2O_5 films [18]. The spectral features allow to establish a phase diagram mapping the effect of substrate temperature on the microstructure evolution of PLD V_2O_5 thin films. RS has also been widely used to study the surface phenomena of electrodes [19,20] and electrolyte including ion-solvent interactions, since the conductivity being proportional to the salt concentration, a correlation between Raman shift and the conductivity of the electrolyte can be established [21,22].

In situ Raman spectroscopy is a direct method for real-time study of dynamic reactions during working conditions of electrochemical cells. Four spectral evolutions can be distinguished as (i) appearance of new band, (ii) shift of vibrational mode, (iii) change in band profile and (iv) change in band intensities (Figure 1). *In situ* RS has been widely employed to elucidate the structural changes at the level of chemical bonds in electrode materials for lithium-ion batteries during the cycling of electrochemical cell; this analytical method is currently used to describe the variations in the valence state of transition-metal cations, lithium transport mechanism (insertion/deinsertion reaction), cycle-induced degradation, electrode–electrolyte interface evolution and state-of-charge (SOC) distribution as well [4,23]. Kinetic characterizations of Li^+ insertion/extraction into/from composite cathode were also investigated by *in situ* Raman spectroscopy [24]. *In situ* RS is currently used to investigate the electrode–electrolyte interface in lithium batteries [25]. Taking the advantages in the difference in Raman spectra vs. composition or/and local symmetry, it is possible to study the spatial distribution of phases in an electrode by mapping [26]. The powerful advantage of *in situ* micro-Raman spectroscopy for the analysis of materials included in a lithium battery was emphasized by several authors [27–29].

The purpose of this review is to acknowledge the current state-of-the-art and the progress of *in situ* Raman spectroscopy that has been made on all the elements of the lithium-ion batteries: cathode and anode materials and the formation of solid electrolyte interphase (SEI) layer. We also discuss the results in the perspective of spatial and real-time investigations by *in situ* Raman imaging (mapping) during charge/discharge cycling.

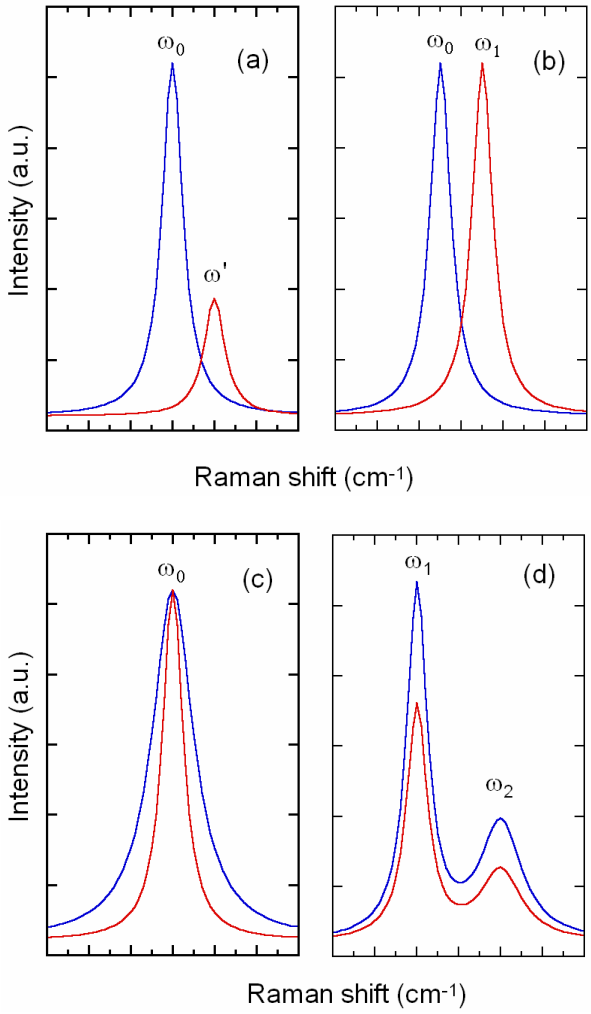

Figure 1. Schematic representation of spectral evolutions investigated by *in situ* Raman spectro-electrochemistry: (a) appearance of new band, (b) shift of vibrational mode, (c) change in band profile and (d) change in band intensities.

2. Raman single point and mapping measurements

2.1. In situ Raman single point

Typical *in situ* Raman spectroscopy is carried out using a confocal Raman spectrometer in backscattering geometry. For a description of the micro-Raman set-up, we guide the reader to the review papers Refs. [28,29]. Typical home-made electrochemical cells for *in situ* Raman studies were targeted to meet their experimental measurements [30–33]. Burba and Frech [30] described a spectro-electrochemical cell that was a modified industrially available coin cell with a 2-mm diameter hole drilled into the coin cell casing (Figure 2a). *In situ* RS cells are currently equipped with a glass, quartz or sapphire window transparent to the Raman laser light. A 100 × magnification long working distance optical objective is used, providing a laser spot of approximately 3 μm^2 on the sample electrode. Another in-situ cell was fabricated using the Swagelok standard [32] with a sapphire optical window (Figure 2b). A home-made *in situ* cell by Novák et al. [34] is presented in

Figure 2c. Industry-standard 2032-coin cells (from Pred Materials International) were adapted to carried out *in situ* Raman mapping of electrode materials (Figures 2d,e). Fang et al. used a MgO window to cover a drilled 1/8 inch diameter hole. State-of-charge maps were collected of a $35 \times 35\ \mu m^2$ area considering two spectral features, i.e., Raman peak position and peak intensity [35]. Ghanty et al. [36] fabricated a *in situ* Raman pouch cell with an optical sodium borosilicate window covering an aperture in the aluminum-coated polyamide outer shell (Figure 2f).

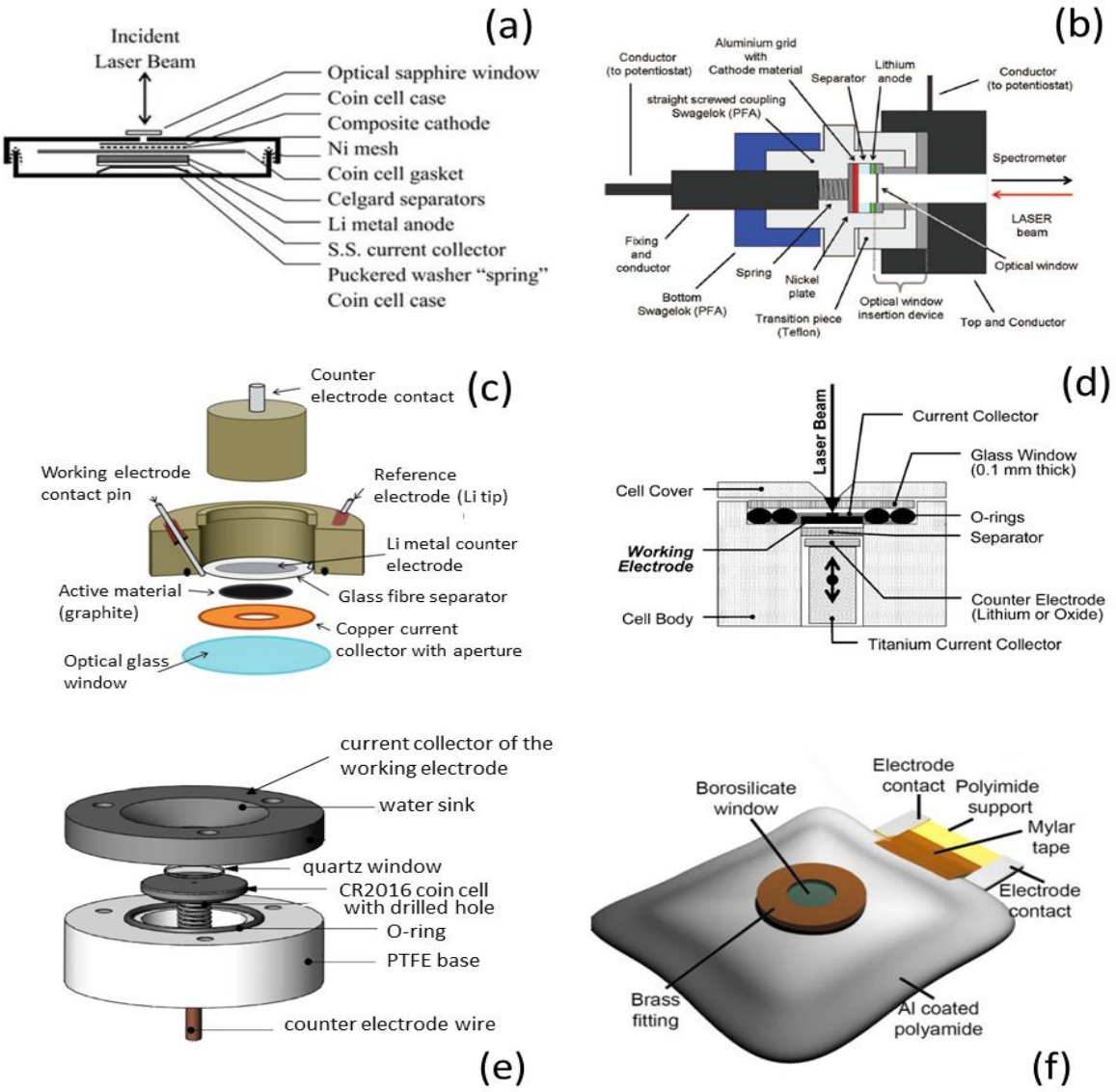

Figure 2. Cross section of home-made *in situ* Raman spectro-electrochemical cells (not drawn to scale): (a) Modified coin cells with a 2-mm diameter hole for *in situ* Raman spectro-electrochemical measurements of $Li(x)V_2O_5$ for lithium rechargeable batteries. From Ref. [30]. (b) Swagelok-type cell with sapphire optical window from Ref. [31]. (c) Schematic *in situ* Raman cell for the study of Li^+ ion intercalation in graphite negative electrode. From Ref. [33]. (d) home-made cell design with glass window. From Ref. [34]. (e) in-situ setup with CR2016 coin cell adapted with quartz window. From Ref. [37]. (f) pouch cell with borosilicate window. From Ref. [36].

2.2. Optical-skin depth

A Raman spectrum represents the response of nanoparticles contained in the volume defined by the focal spot times the penetration depth δ_p that depends on the probed sample. The axial resolution in opaque materials is determined by the optical-skin depth (δ_p) of the laser beam penetrating into a material. Because of the optical absorption of the light in electrode materials, the observed Raman spectra are induced in a thin surface layer; thus, due to small δ_p value, Raman spectroscopy can be considered as a surface analytical method in most cases. The Raman scattering intensity is then weak because of the small material volume probed ($V < 1$ μm^3). The skin depth is given by the relation:

$$\delta_p = (2\lambda/\mu\sigma)^{1/2} \quad (1)$$

where λ is the laser wavelength, σ the electronic conductivity and μ the magnetic permeability.

Consequently, using laser excitation with higher wavelength increases the penetration depth and an increase in the electronic conductivity, e.g., from semiconductor to metal, results in decrease of δ_p. According to the Beer–Lambert law, the intensity $I(\xi)$ of the laser light inside the materials is an exponential function of the absorption coefficient α of the material as $I(\xi) = I_0\exp[-\alpha\xi]$. The optical penetration depth defined as the distance at which the intensity decreases to 1/*e* (37%), where *e* is the base of the natural system of logarithms, we have $\delta_p = \alpha^{-1}$. For instance, $\delta_p \approx 1$ μm in crystalline silicon, $\delta_p \approx 100$ nm in amorphous silicon and $\delta_p \approx 100$ nm in Li_xSi [38–40]. Currently, the experiments are performed at very low laser power $W_{laser} \approx 0.02$ mW using a 0.1% filter that corresponds to a specific power of 600 W cm^{-2}. An optical-skin depth is less than 50 nm in highly oriented pyrolytic graphite examined with a 514.5 nm green laser beam [41], while δ_p falls to few nanometers in delithiated $Li_{1-x}Ni_{1/3}Mn_{1/3}Co_{1/3}O_2$. Another experimental case is the low optical-skin depth ($\delta_p \approx 30$ nm) of carbon coating onto $LiFePO_4$ particles [42,43]. Thus, to probe the electrode materials of LIBs, the choice of laser excitation line at high wavelength $\lambda > 700$ nm is preferred, rather than the solid-state 532 nm excitation.

2.3. In situ Raman imaging

In situ Raman mapping consists in the spatial characterization of an electrode at a multitude of locations that allows to define the chemical distribution and inhomogeneity of particles during the cell charge–discharge process and electrode degradation as well. A Raman image is formed by hyperspectral data set, in which a pixel is a complete Raman spectrum. Raman micro-spectroscopy as a spatially resolved analytical method is currently used to generate local surface images, to construct state-of-charge maps of electrodes, or to investigate the kinetic aspect of Li^+ intercalation–deintercalation process in a single particle. The feasibility of Raman mapping was first explored by Panitz et al. [44] who investigated the lithium intercalation in graphite electrode under potentiostatic and galvanostatic conditions. Results indicated that, at a potential of 0.2 V vs. Li^+/Li, the lithium is not homogeneously inserted over the graphite electrode and a new Raman band evolved at ca. 1850 cm^{-1} at potential 0.18 V vs. Li^+/Li. The same group developed an in-situ cell to monitor the Li insertion in carbon electrode by changing the optical geometry that improved the signal-to noise ratio by a factor of 20 [45]. The mapping of the state-of-charge distribution of $LiCoO_2$ (LCO) was investigated with a special resolution of few micrometers, which enabled to test the intensity, width and position of the Raman peaks by constructing the Raman images of the A_{1g} mode (595 cm^{-1}) [46].

The remarkable potential of Raman imaging was applied to study the local degradation behavior in composite cathode materials such as $LiNi_{0.8}Co_{0.15}Al_{0.05}O_2$ and $LiNi_{0.33}Mn_{0.33}Co_{0.33}O_2$ [47]. The authors investigated the nanoscale modifications of the surface composition, structure, SOC, and determined the electronic conductivity at the electrode surface as well. Raman imaging was performed on an area of 52×75 μm^2 at 0.7 μm resolution. An image is formed of color-coded pixels, which represent the relative intensities of specific Raman peaks and the chemical surface composition, i.e., active material and carbonaceous additive (acetylene black, graphite, etc.) characterized by the Raman G- and D-bands. Currently, the Raman spectrum of an electrode particle varies significantly with the position on the surface. For example, the spectrum of $LiNi_{0.33}Mn_{0.33}Co_{0.33}O_2$ displays bands at 475 and 554 cm^{-1} associated with the vibrations of the Ni–O bonds having intensities strongly coupled with electronic states that provoke Raman resonance behavior. Consequently, the relative intensities I_{475}/I_{554} vary significantly from one particle to another. Fang et al. [35] adapted industry-standard coin cells for high spatial resolving *in situ* Raman mapping. By extraction of the local frequency of the A_{1g} mode of electrodes with rock-salt-type structure, the authors demonstrated an easy-to-implement electrode design using $LiNi_{0.5}Mn_{0.3}Co_{0.2}O_2$ (NMC) as active material.

Quantification of the Li^+ ion transport in liquid electrolyte, i.e., $LiClO_4$ dissolved in dimethyl carbonate (DMC), was performed by combining high-spatial-resolution confocal Raman microscopy and microfluidic technique. [48]. The Raman peak at ca. 523 cm^{-1} corresponding to the O–C–O deformation mode of DMC develops a sideband with the increase of $LiClO_4$ concentration. Its analysis using a Voigt profile was used to quantify the ionic diffuse transport.

Using high-speed and high-definition *in situ* Raman imaging, several groups have investigated the local SOC and state-of-health (SOH) distribution of electrodes. Nishi et al. [49] visualized the SOC distribution in $LiCoO_2$ at various rates and showed the limitation of ionic transport. Nanda et al. [50] investigated the SOC inhomogeneity in fresh and aged layered cathodes, while Slautin et al. [51] studied the degradation paths in $LiMn_2O_4$ spinel structures. As an example of experimental procedure, Raman maps of the $LiNi_{0.8}Co_{0.15}Al_{0.05}O_2$ (NCA) positive electrode were performed by collecting spectra in a range of Raman shift from 250 to 1800 cm^{-1} across a 10 μm square region of the electrode surface [50]. Results obtained from the composite electrode NCA + carbon black + PVdF binder are shown in Figure 3. Typical map is obtained with a minimum of 1000 data points. Each spectrum was treated considering three Raman peaks of NCA centered at ca. 475, 550 and 620 cm^{-1} attributed to the vibrations of Ni–O bonds, while bands of the carbon are observed at ~1350 cm^{-1} (D band), 1500 cm^{-1} (amorphous carbon) and 1590 cm^{-1} (G band).

3. Positive electrode (cathode) materials

3.1. Rock-salt-type compounds

Structural properties of layered-type compounds such as $LiCoO_2$, $LiNiO_2$, $LiNi_xCo_{1-x}O_2$, $LiNi_{0.8}Co_{0.1.5}Al_{0.05}O_2$ as well as $LiNi_xMn_yCo_zO_2$ with various Co contents were widely investigated by *in situ* X-ray diffraction [52]. These compounds crystallize with a lamellar structure of rock-salt-type of *R*-3*m* space group. For instance, the poor electrochemical cycling behavior of Ni-rich NMC ($LiNi_{0.5}Mn_{0.2}Co_{0.3}O_2$) cathode is due to the structural phase transition between hexagonal phases H2

to another hexagonal phase H3 (at 4.7 V) upon Li^+ de-intercalation, which can be suppressed in long-term cycleability.

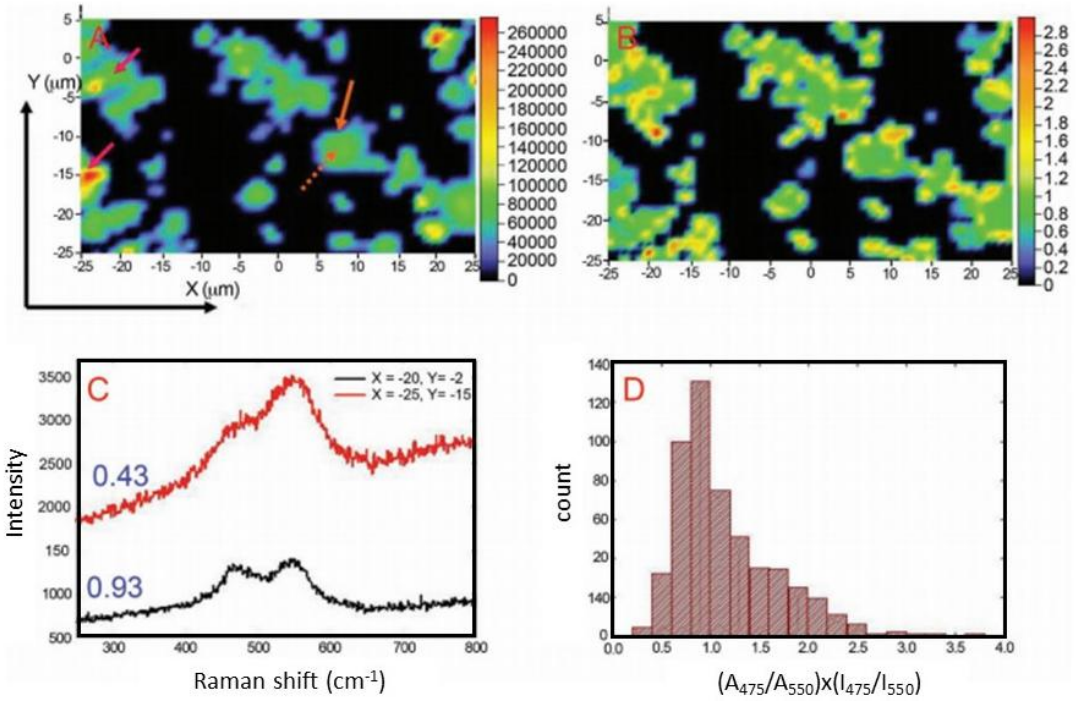

Figure 3. Raman mapping and SOC surface analysis of NCA composite cathode. (a) Map showing the spectral intensity as the total area under the NCA Raman peaks. The solid (orange) arrow points to NCA particle interior and the dotted arrow points to interface between particle and carbon-filled binder. (b) SOC map derived from analysis of NCA Raman peaks. (c) Representative Raman spectra of the NCA active particles indicated by the red arrows for two values of the SOC parameter. (d) Histogram showing the frequency distribution of the SOC parameter. The quantity on the abscissa $(A_{475}/A_{550}) \times (I_{475}/I_{550})$ is a measure of the SOC, as described in the text. Electrode was charged galvanostatically to 4.2 V at 3C rate without any potentiostatic step. Reprinted by permission from Ref. [50].

3.1.1. $LiCoO_2$ (LCO)

$LiCoO_2$ prepared by solid-state reaction or by wet chemistry followed by a post-annealing treatment at 800–900 °C (denoted HT-LCO) crystallizes in the rhombohedral system *R*-3*m* with the α-$NaFeO_2$ structure built by alternating ordered layers of CoO_6 and LiO_6 octahedra along the c-axis. At a lower annealing temperature, $T_a \approx 400$ °C, LCO crystallizes in the cubic NaCl-type structure (*Fd*3*m* space group) (LT-LCO) with cations distributed among octahedral sites of the cubic oxygen close-packed array. While the HT- and LT-LCO structures cannot be efficiently discriminated by X-ray diffraction, Raman spectroscopy has been successful to determine the phase of $LiCoO_2$ synthesized in the temperature range 400–900 °C [16].

3.1.1.1. Phase identification of $Li_{1-x}CoO_2$

The phase identification of $Li_{1-x}CoO_2$ as a function of the Li extraction is currently established via the A_{1g} and E_g phonon Raman active (gerade) modes (Table 1), which are observed at 596 and 487 cm^{-1}, respectively. The A_{1g} mode is the symmetrical stretching of Co–O (atomic displacement parallel to *c*-axis) whereas the E_g mode is the symmetrical deformation (atomic displacement perpendicular to *c*-axis). Gross and Hess [32] demonstrated the presence of the resonance Raman effect for $LiCoO_2$ cathode under electrochemical conditions upon switching the laser excitation by evaluating the A_{1g}/E_g integrated intensity ratio. A_{1g}/E_g increases from 0.9 (for λ = 632.8 nm) to 2.3 (for λ = 532 nm) due to resonance process involving the *d–d* electronic transition from Co-t_{2g} to Co-e_g bands (optical absorption at 2.1 eV (591 nm)) and under resonance conditions an overtone of the A_{1g} band occurs [12]. The resonance enhancement for LCO materials was also pointed out when using a green laser excitation for *in situ* studies [32].

Table 1. Atomic position, site symmetries and Raman active modes for LT- and HT-$LiCoO_2$ compounds.

Space group	Atom	Wyckoff positions	Raman modes
R-3*m*	Li (0,0,½)	3*b*	$A_{1g} + E_g$
	Co (0,0,0)	3*a*	
	O (0,0,¼)	6*c*	
*Fd*3*m*	Li (0,0,0)	16*c*	$A_{1g} + E_g + 2F_{2g}$
	Co (½,½,½)	16*d*	
	O (¼,¼,¼)	32*e*	

Several articles have reported *in situ* RS experiments of LCO electrode materials [2,14,20,31,32,53–59] but only few of them mentioned the phase transformation upon lithium extraction/insertion. The early work by Inaba et al. [20] showed the change in the Raman spectra of $Li_{1-x}CoO_2$ prepared by electrochemical extraction of Li ions. Results indicated a line broadening of a second hexagonal phase and the monoclinic phase. Novák et al. [2] addressed the rapid disappearance of the A_{1g} band with increasing potential (V > 3.95 V). This Raman band emerges again on discharge (at ca. 3.7 V) with a lower intensity, which was attributed to a lithium-deficient LCO electrode.

As shown in Figure 4, the phase evolution during the charge of $Li_{1-x}CoO_2$ (lithium extraction) is as follows: (i) for $0 \leq x \leq 0.1$ the two phonon (normal) modes at 596 and 487 cm^{-1} are invariant and correspond to the hexagonal H1 phase, (ii) two new Raman bands located at 473 and 572 cm^{-1} appear at $x > 0.1$ due to the formation of the hexagonal H2 phase that coexists with H1 up to $x \approx 0.3$, i.e., in a two-phase system, (iii) for $x > 0.3$ the LCO-type normal modes disappeared while the modes of the H2 phase shift toward lower wavenumbers to 462 and 567 cm^{-1}, respectively, due to the expansion of the Co–O bonds along the *c*-axis (Figure 5). It is worthy to note that the intensities of the Raman peaks decrease significantly due to the transition from semiconductor to metal for $x > 0.15$. Novák et al. [2] suggested an increase of electrical conductivity by about two orders of magnitude in $Li_{1-x}CoO_2$ for $x > 0.04$ correlated with the change of colour of the particles from dark to light. Similar description was previously reported by Inaba et al. [20], while Itoh et al. [14]

conceived the formation of a Raman-inactive phase. Song et al. [15] investigated the phase change of LCO films deposited on to Co substrate using a spot of 1 μm of 514.5 nm laser irradiation by *in situ* RS. A remarkable phase change of the hexagonal film deposited at 200 ℃ to cubic spinel is due to reaction of LCO films with the Co substrate forming a Co-rich phase or Li deficient phase $Li_{1-x}CoO_2$. The laser power (≤50 mW cm^{-2}) provokes a shift accompanied by broadening and depressed intensity of the hexagonal A_{1g} (589 cm^{-1}) and E_g (478 cm^{-1}) bands, and the occurrence of two new bands at ca. 523 and 681 cm^{-1} that correspond to the cubic spinel *Fd*3*m* phase. In the harmonic approximation, the phonon frequencies are given by:

$$v \approx (k/\mu)^{1/2} \tag{2}$$

where k is the force constant and μ the reduced mass ($\mu^{-1} = m_{Li}^{-1} + (2m_O)^{-1}$). As Li and Co co-exist in the Li sites, μ becomes larger, which results in band softening and broadening. Such a structural transformation has been confirmed by FTIR and RS spectroscopy of sol-gel LCO powders [60] showing the growth of the rock-salt structure (*R*-3*m* symmetry) upon annealing heat-treatment in the range 400–900 ℃. Upon prolonged cycling, degradation of LCO cathodes is evidenced by disappearance of the peak at 579 cm^{-1} and the emergence of new bands at 515 and 674 cm^{-1} assigned to the mode vibration of Li_2O and Co_3O_4, respectively, both being electrochemically inactive components [61].

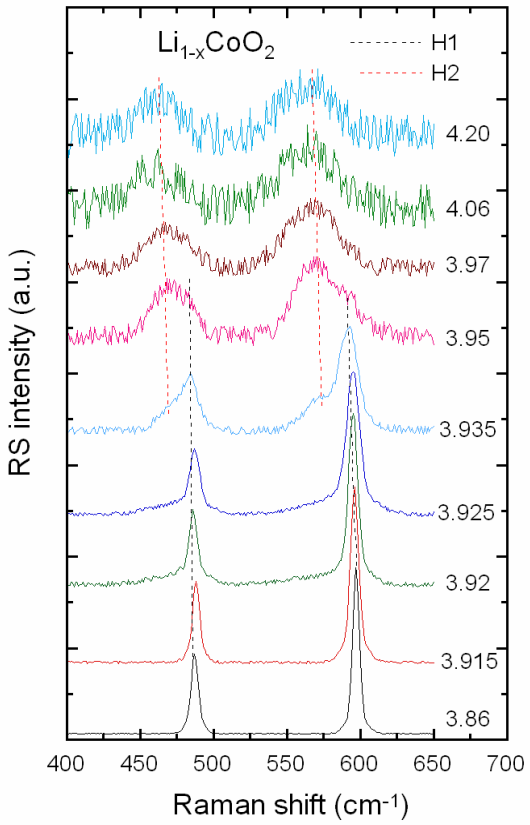

Figure 4. Raman spectra of the $Li_{1-x}CoO_2$ electrode recorded during the charge process.

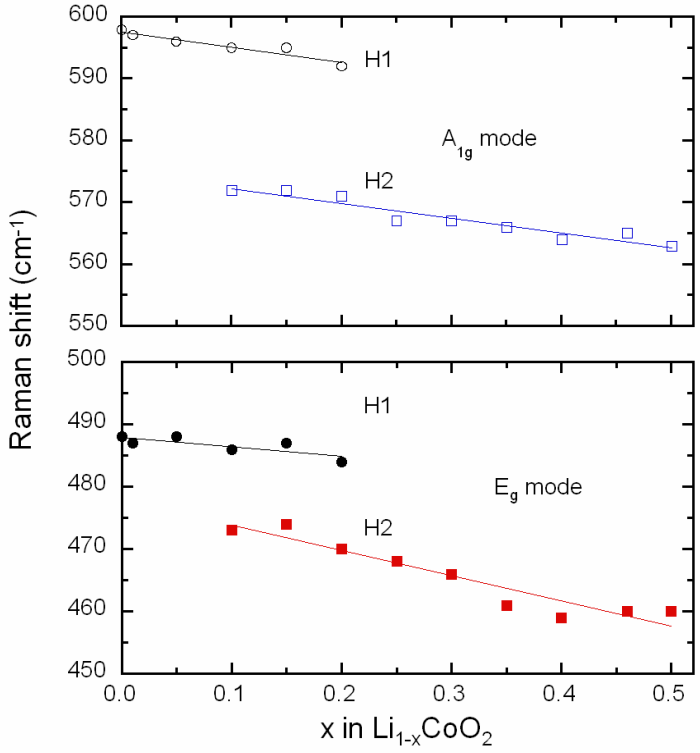

Figure 5. Phase diagram of the $Li_{1-x}CoO_2$ electrode.

3.1.1.2. Surface modification upon cycling

Spatially-resolved *in situ* Raman diagnostics were performed to analyze the variation of chemical composition of composite electrodes based on the mixture of LCO active particles, carbon additive and polyvinylidene fluoride (PVdF) binder, and the degradation mechanism of materials [12,56,58]. Taking into account the resonance enhancement for LCO materials, i.e., maximum for green laser excitation, the wavelength-dependent spatially resolved analysis demonstrated significant variation of chemical composition across the electrode surface [32]. Using the same technique, Fukumitsu et al. [57] investigated the SOC distribution in cross-section of $LiCoO_2$ cathode and observed the inhomogeneity of the active particles where Li^+ ions did not completely return after discharging. Such an inhomogeneous distribution and the mapping of the LCO electrode degradation were also correlated with battery performance by several groups [31,55–57]. Hausbrand et al. [12] addressed the degradation aspects upon overcharge of $LiCoO_2$/PVdF/carbon black composite (85:10:5) electrodes by *in situ* RS imaging the A_{1g} phonon band of LCO. After cycling at C/12 rate, the composite electrode showed a redistribution of the chemical composition that consists in the formation of surface layers; thus, the loss of electrical contact between LCO particles were evidenced by mapping, while Gross and Hess claimed no significant structural changes observed from *in situ* RS experiments [32]. Nishi et al. [49] investigated the local SOC distribution of LCO cathode. The results showed that individual LCO particles were discharged at various rates with inhomogeneous current distribution and part of them was irreversibly charged upon subsequent cycles due to the increasing electrical resistance between

LCO grains. As an example, Figure 6 displays the Raman images recorded during the first and second cycle of LCO (charge at 0.4C and discharge at 1C) in the potential range 2.5–4.4 V vs. Li^+/Li. This electrode shows an inhomogeneous distribution of the SOC of the particles upon cycling.

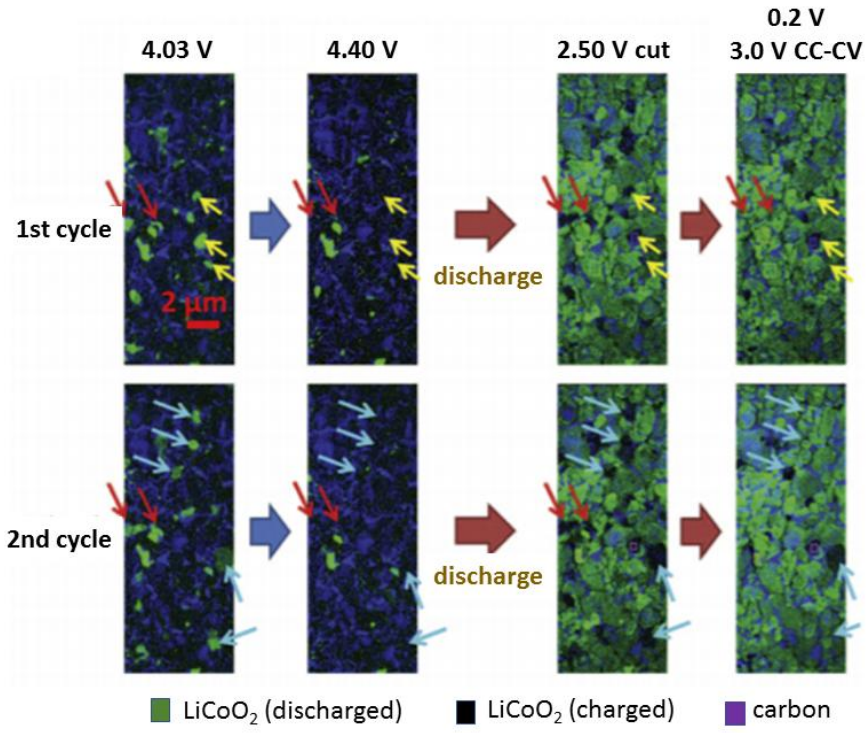

Figure 6. Raman images recorded during the first and second cycle of LCO (charge at 0.4C and discharge at 1C) in the potential range 2.5–4.4 V vs. Li^+/Li. The SOC distribution is indicated by arrows: particles charged and discharged at slower rate during both cycles (red), particles charged at slower rate in the first cycle (yellow) and particles charged and discharged at normal rate during the first cycle but at a slower rate in the second cycle (blue). Reprinted by permission from Ref. [49].

Recently, Otoyama et al. [59] reported the Raman mapping of the composite electrode, i.e., mixture of active $LiCoO_2$ and $Li_2S–P_2S_5$ solid electrolyte before and after the initial charging reaction. While the Raman images show the expected distribution of reactions after full charge test, several LCO particles do not display structural changes. Kostecki et al. [47] reported similar studies performed on $LiNi_{0.8}Co_{0.15}Al_{0.05}O_2$ (NCA) composite cathode material. Observation of the Raman microscopy mapping of the electrode surface showing nonuniform electrode state-of-charge was correlated with the significant impedance rise and capacity fade of the lithium-ion cell graphite//NCA.

3.1.2. Mixed layered oxides $LiNi_aMn_bCo_{1-a-b}O_2$ (NMC)

Mixed layered oxides, namely lithium nickel-manganese-cobalt oxides $LiNi_aMn_bCo_cO_2$ with $c = 1 - a - b$ (named NMC) are solid solutions of the binary $LiMO_2$ (M = Ni, Mn, Co) compounds.

They are identified by the cation stoichiometry, for instance NMC532 for $LiNi_{0.5}Mn_{0.3}Co_{0.2}O_2$. NMC materials crystallize with the α-$NaFeO_2$ structure belonging to the *R*-3*m* (D_{3d}^5) space group. The local structure of $LiNi_{1/3}Mn_{1/3}Co_{1/3}O_2$ (NMC333) synthesized by wet chemistry with various chelate to metal-ion ratio was studied Raman spectroscopy [62]. Analysis of the intensity A_{1g} and E_g modes by integral of the Lorentzian individual band allows to estimate the cationic mixing, i.e., partial occupancy of Ni^{2+} in Li sites. The intensity of the Ni–O and O–Ni–O vibrations (ν_1 and ν_4, respectively) are smaller in the sample with higher cationic mixing. The larger width of these ν_1 and ν_4 vibrations means that the lifetime of phonons is shorter, another evidence of the larger Ni cationic disorder, in agreement with the structural analysis. An important issue for NMC materials is the cation mixing, i.e., filling of Li sites by Ni^{2+} ions. Employing a combination of XRD and spectroscopic methods (Raman and NMR spectroscopy), Ben-Kamel et al. [63] reported the effect of varying Co content on the local structure of as-synthesized $LiNi_xCo_yMn_zO_2$ oxides and showed that the cation mixing effect during cycling decreases with increasing Co content, illustrating the usefulness of Raman spectroscopy in this issue. The effect of high voltage charging on NMC532 cathodes has been investigated by *in situ* Raman mapping by analyzing the high-frequency phonon mode. Above the potential 4.4 V vs. Li^+/Li, the Raman component at 595 cm^{-1} shifts above 600 cm^{-1}, which corresponds to a capacity loss similar to the one observed in spinel $LiMn_2O_4$ [64]. The local charging profiles of NMC532 particles during cycling was studied by construction of high-spatial resolved SOC images of 35 μm square portion of electrode. The delithiation process provokes a downshift in the frequency of A_{1g} and E_g peaks, accompanied with a decrease in the A_{1g} peak in intensity and an increase in the E_g peak intensity. The local topography was obtained from data by numerically extracting the frequency that highlights the inhomogeneity in the SOC distribution when the cathode is charged further to 4.21 V [35]. Raman mapping was conducted for NMC333 composite cathode in solid-state batteries. Using $75Li_2S–25P_2S_5$ solid electrolyte, mapping images displayed uniformly delithiated and lithiated NMC particles [65]. The ratio I_{595}/I_{474} was used to determine the electrode state-of-charge with I_{595}/I_{474} = 4.0 for low SOC and I_{595}/I_{474} = 0.85 for high SOC.

In situ Raman spectroscopy of Ni-rich $Li_{1+x}(Ni_yCo_zMn_z)_wO_2$ ($0.005 < x < 0.03$; *y*:*z* = 8:1, *w* is nearly 1) electrodes demonstrated the structural transformation using an original pouch cell with sodium borosilicate glass window [36]. Figure 7a presents the deconvoluted Raman spectrum of a NMC811 electrode in the spectral range of 400–650 cm^{-1}, which shows six active Raman modes according to the approach proposed by Julien and co-workers [63]. *In situ* Raman spectra collected during Li^+ extraction (charge process) in the electrode potential from 3.8 to 4.3 V vs. Li^+/Li are shown in Figure 7b. Spectral changes are correlated with the structural transitions from initial hexagonal phase H1 to phase H2 and to coexisting phases H1 + H2. The bandwidth (FWHM) of A_{1g}(Ni) and E_g(Ni) modes remained unchanged upon the potential charge 3.7–3.8 V corresponding to the H1 phase, while increased up to a maximum at 3.9–4.0 V (phases H1 and H1 + H2) and further decreased in the potential range 4.0–4.3 V implying a structural transition from disorder to order that occurs for $x > 0.56$ in $Li_xNi_{0.8}Mn_{0.1}Co_{0.1}O_2$ electrode. During the discharge, the Raman response shows quite reversible behavior with low deviations from the original ν and FWHM values.

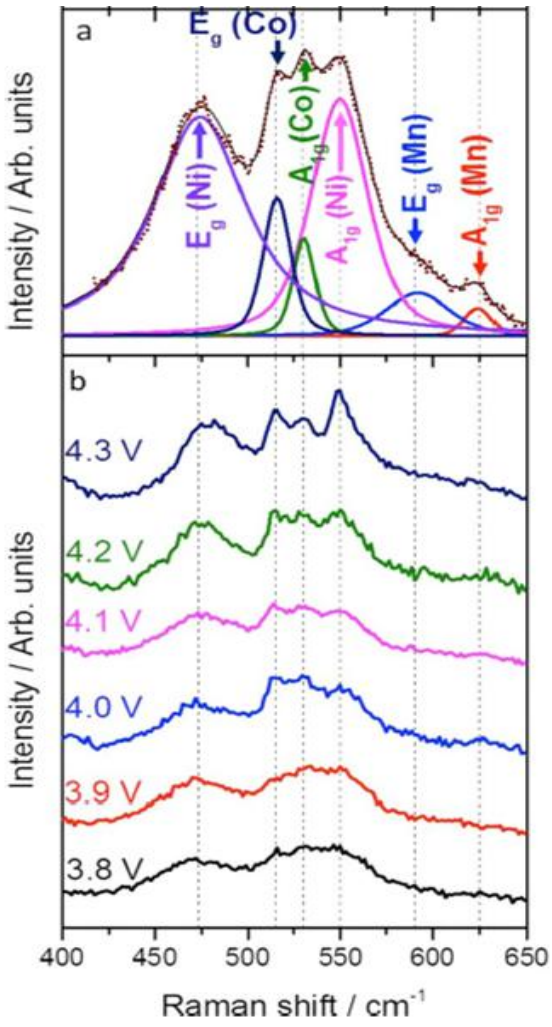

Figure 7. (a) Raman spectrum of a NMC811 electrode with the deconvolution of six vibrational components. (b) *In situ* Raman spectra collected during Li^+ ion extraction (charge process) in the electrode potential from 3.8 to 4.3 V vs. Li^+/Li. Reprinted by permission from Ref. [36].

3.1.3. Li-rich layered–layered oxides (LLNMC)

The exact nature of Li-rich layered-layered cathode materials (LLNMC) of formula $Li_{1+\delta}(Ni_aMn_bCo_{1-a-b})_{1-\delta}O_2$ or xLi_2MnO_3 $(1 - x)LiMO_2$ (with M = Ni, Mn, Co) is still the subject of debate; two models are proposed, one considering the structure of a lamellar compound with Li_2MnO_3 domains, the other proposing a solid solution as an integrated structure of Li_2MnO_3 ($C2/m$) and $LiMO_2$ (R-3m) layered components. For $\delta > 0$, the overlithiated oxide are also known as high-energy NMC (HE-NMC). Li_2MnO_3 is electrochemically activated during the first charge at a potential plateau of 4.5 V. Depending on the composition and charging conditions, LLNMC is enabling to deliver more than 250 mAh g^{-1} at potential of 5 V vs. Li^+/Li. This class of materials is often noted xLi_2MnO_3 $(1 - x)LiMO_2$ based on the X-ray diffraction patterns. Among this series, $0.5Li_2MnO_3$ $0.5LiNi_{0.5}Mn_{0.5}O_2$ is equivalent to $Li_{1.2}Ni_{0.2}Mn_{0.6}O_2$ and $0.5Li_2MnO_3$ $0.5LiNi_{0.33}Mn_{0.33}Co_{0.33}O_2$ to $Li_{1.2}Mn_{0.54}Ni_{0.13}Co_{0.13}O_2$. Both of them are promising

cathode materials. The layered structure of Li_2MnO_3 or $Li(Li_{1/3}Mn_{2/3})O_2$ is described in the monoclinic $C2/m$ (C_{2h}^3) space group; there is an extended cation ordering in the slabs with the Li/Mn ratio of 1/2 with Li ions fully occupying one 2*b* Wyckoff site of the slabs along the *c*-axis, while Mn ions occupy the 4*g* site. Factor group analysis predicts 15 Raman active modes as $7A_g + 8B_g$.

Lanz et al. [66] stated that, prior to charging, i.e., in the open-circuit voltage (OCV) state, the LLNMC framework is a mixture of the Li_2MnO_3 and layered $LiMO_2$ phases observed by *in situ* XRD and *in situ* Raman spectroscopy. The local structure of Li-rich NMC with the composition $Li_{1.20}Mn_{0.54}Co_{0.13}Ni_{0.13}O_2$ studied by Raman spectroscopy was compared with that of layered compounds $LiCoO_2$, $LiNi_{1/3}Mn_{1/3}Co_{1/3}O_2$ and $Li(Li_{1/3}Mn_{2/3})O_2$ (or Li_2MnO_3). This comparison supports that $Li_{1.20}Mn_{0.54}Co_{0.13}Ni_{0.13}O_2$ is a solid solution of Li_2MnO_3 and $LiNi_{1/3}Mn_{1/3}Co_{1/3}O_2$ instead of separated domains of these components [67]. However, an additional Raman peak located at ~660 cm^{-1} was attributed to the vibrational mode of Mn–O bond also observed in other layered phases such as HT-$Li_{0.52}MnO_{2.1}$(with $I4_1/amd$ symmetry) [68] simply shifted by the fact that the Mn–O bond is shorter in LLNMC.

In situ Raman spectroscopy of Li-rich layered oxides $xLi_2MnO_3 \cdot (1-x)LiMO_2$ (*M* = Ni, Co, Mn) was carried out for several compositions *x* = 0.3, 0.5, and 0.7 [37,66,69–73]. The general trends consisted in the determination of the Li_2MnO_3 activation during the first cycle characterized by a modification of the ionic local coordination and an increase of the ionic disorder of the Li-rich layered structure. Singh et al. [69] reported *in situ* Raman spectra of $Li_{1.2}Ni_{0.175}Co_{0.1}Mn_{0.52}O_2$ during galvanostatic charge and discharge process between OCV (~3.0 V) and 4.8 V. During the charge, a new peak emerges at ~544 cm^{-1} due to the oxidation of Ni^{2+} ions, and a change in the Raman peak at 445 cm^{-1} (up to 4.1 V) reflects the extraction of Li^+ ions from the transition-metal layer, contrary to the previous claim of a movement of Li^+ ions to vacant site at lower potential 2.92 V [74]. It was concluded that, in the voltage range 4.1–4.4 V, lithium ions are removed from both the transition-metal layers and lithium layers. At upper state of charge at 4.55–4.6 V, the oxygen removal becomes severe, and associated with the diffusion of the transition metal ions into the vacant sites. *In situ* Raman spectroscopy was applied to characterize the electrochemical activation of Li_2MnO_3 in LLNMC cathodes. The fingerprint of this activation lies in the main peak at 615 cm^{-1} (A_g band of Li_2MnO_3 phase), which shifts to higher wavenumbers ~630 cm^{-1} upon of charging above 4.4 V vs. Li^+/Li [70]. The same group of researchers reported the emergence of the new Raman band at ~545 cm^{-1} for stoichiometric $Li_{1.1}(Ni_{1/3}Co_{1/3}Mn_{1/3})O_{2.1}$ during the first charging process at low voltage in the range 4.1–4.3 V vs. Li^+/Li. The activation of Li_2MnO_3 possibly results in the formation of Li_2O and MnO_2, the former being responsible for the band at ~545 cm^{-1} [66]. This assumption was previously proposed by Hy et al. [72] by studying the oxygen-related surface reactions occurring on $Li_{1.2}Ni_{02}Mn_{0.6}O_2$ using in-situ surface enhanced Raman spectroscopy (SERS). Li_2O was directly detected during the extended voltage plateau at 4.5 V that leads to the hydrolysis of the electrolyte and the formation of Li_2CO_3. Rao et al. [71] reported the spectral modifications of the $Li_{1.2}Mn_{0.54}Ni_{0.13}Co_{0.13}O_2$ electrode during charging from OCV to 4.7 V (Figure 8). While the Raman spectrum is invariant until the charge at 4.2 V, a new broad peak due to the Ni^{3+}–O bonds appears at ca. 542 cm^{-1} at 4.25 V, which becomes sharp in the potential range 4.35–4.47 V. Other notable changes associated with the removal of Li^+ ions consist in the vanished 445 cm^{-1} peak and a shift of the 490 cm^{-1} peak due to the increase of the interlayer distance. Finally, in the potential region 4.25–4.5 V, a strong increase of the Raman signal background is attributed to the Li_2MnO_3 activation indicating a local environment modification with simultaneous lithium extraction and oxygen release.

During discharge, the Raman spectrum returns to the initial situation with suppression of the background intensity of the peak.

Particular attention has been devoted to the effects of cycling on the structure of lithium-rich NMC cathode compounds, and of Li_2MnO_3–Li$M$$O_2$ (M = Ni, Mn, Co) composites (LR-NMC), the later being an integrated structure of the $C2/m$ (Li_2MnO_3) and R-3m (Li$M$$O_2$) layered components. Several investigators have shown the gradual transformation of Li-rich NMC materials cycled from a discharge state at 2.0 V to the charging voltage as high as 4.9 V [75,76]. Using a combination of XRD, TEM and ex situ Raman spectroscopy, Amalraj et al. [75] demonstrated a partial layered-spinel structural transition in the initial charge to 4.7 V vs. Li^+/Li. Similar results on carbon coated $Li_{1.2}Mn_{0.56}Ni_{0.16}Co_{0.08}O_2$ were reported by Kumar-Nayak et al. [76]. The Li-rich NMC Raman features were interpreted in terms of a gradual layered to spinel transformation provoked by electrochemical cycling.

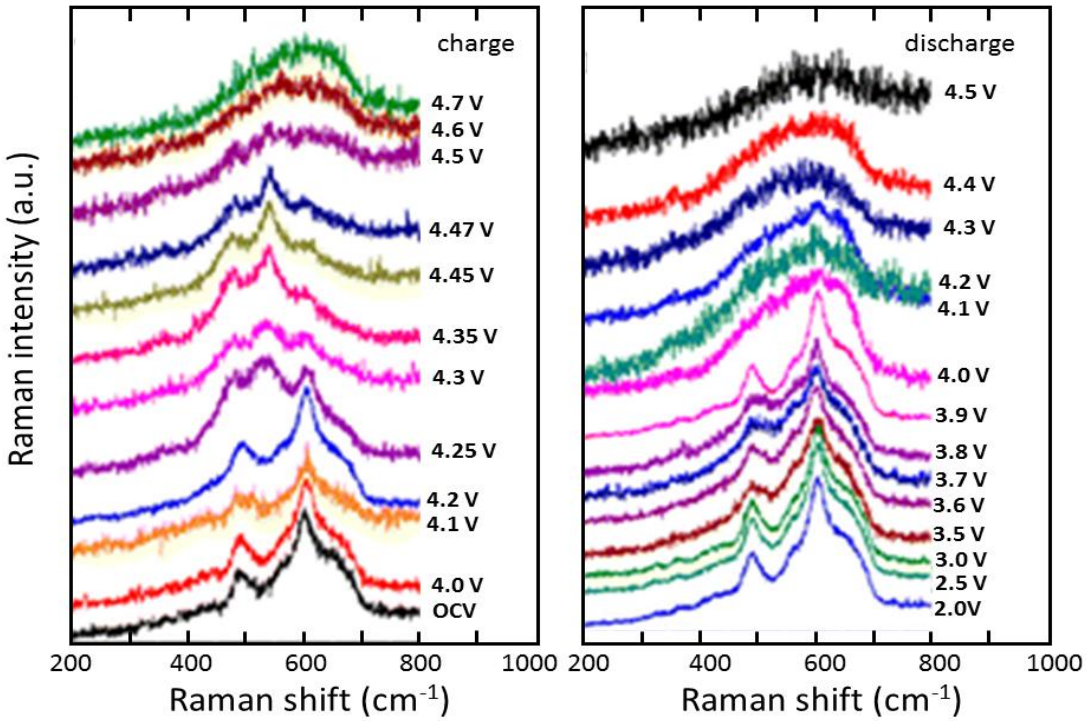

Figure 8. *In situ* Raman spectra of $Li_{1.2}Mn_{0.54}Ni_{0.13}Co_{0.13}O_2$ cathode cycled at C/20 rate. Reprinted by permission from Ref. [71].

Long-term cycling of high-energy sol-gel synthesized cathodes, i.e., Li-rich layered-layered oxides xLi_2MnO_3 $(1-x)LiNi_{2/3}Co_{1/6}Mn_{1/6}O_2$ (x = 0.3, 0.5 and 0.7) was investigated by *in situ* Raman spectroscopy for 35 cycles. During the rate capability measurements at different current densities, the A_{1g} (602 cm^{-1}) and E_g (490 cm^{-1}) phonon modes were unchanged without the occurrence of 630–670 cm^{-1} peaks corresponding to the phonons mode of the cubic spinel-like phase. The increase of the bandwidth of the phonon modes after electrochemical tests was attributed to the formation of the SEI layer [73]. Huang et al. [37] reported similar behavior and showed that, using in-situ electrochemical Raman spectroscopy correlated with the differential capacity (dQ/dV) curves, the

oxidation reactions $Ni^{2+} \rightarrow Ni^{3+} \rightarrow Ni^{4+}$ appeared in the potential range 3.70–4.45 V with a good reversibility in Li-rich $0.5LiNi_{0.5}Mn_{0.5}O_2$ $0.5Li_2MnO_3$ material. Recently, the study of the fate of Li_2MnO_3 (*C*2/*m*) from a commercially produced LLNMC cathode material having the composition $0.49Li_2MnO_3$ $0.51LiNi_{0.37}Co_{0.24}Mn_{0.39}O_2$ (Toda Kogyo Corp. HE5050) adopted the domain model. The best spectral response in terms of signal-to-noise, was obtained using the 785 nm laser excitation rather than lower wavelengths [77]. On charge, the *C*2/*m* phase was delithiated at the same rate as the *R*-3*m* phase, while on discharge the monoclinic component was reformed latter.

3.1.4. $LiNi_{0.8}Co_{0.15}Al_{0.05}O_2$ (NCA)

Aluminum-doped Ni-rich layered structure, i.e., $LiNi_{0.8}Co_{0.15}Al_{0.05}O_2$ (named NCA) is considered as a promising cathode material for high-power batteries with a high specific discharge capacity of ~180 mAh g^{-1} at 1C-rate and a superior thermal stability [78]. Increase of the Li^+ ion diffusivity in the layered *R*-3*m* lattice is due to the aluminum substitution which enlarges the c-axis parameter [79]. *In situ* Raman microscopy was investigated to evaluate the kinetic features of Li extraction/insertion of individual NCA particles [24], the SOC distribution for deep discharge regime [47], and the NCA electrode degradation upon long term cycling [11]. Using a sealed spectro-electrochemical cell, *in situ* monitoring of the SOC of NCA composite electrodes (84 wt% NCA, 4 wt% carbon black, 4 wt% SFG-6 graphite and 8 wt% PVdF) showed that the rate of charge and discharge of a selected particle is dependent of the time of the process and location in the electrode. *In situ* Raman spectra collected using the 632 nm laser line are dominated by a group of bands in the spectral range 470–580 cm^{-1} characteristic of the Ni–O bonds in NCA oxides. It is assumed that the integrated peak ratio I_{475}/I_{553} is proportional to the amount of lithium in one particle, which allows the measure of SOC in individual particle. However, the plot of I_{475}/I_{553} versus electrode potential does not show symmetric behavior during charge-discharge cycle, due to the non-uniform particle distribution [24].

Performing Raman microscopy mapping of NCA cathode material in a pouch-type lithium-ion cell, Kostecki et al. [47] showed that the SOC distribution of particles was non-homogeneous despite the cycling at deep discharge regime. The NCA electrode degradation upon long term cycling was also studied by the same group [11]. Raman image was collected on an area 52 μm × 75 μm using the red excitation source (632.8 nm) with a spot of ~1.2 μm of power adjusted at 0.1 mW exhibiting the Raman features of NCA (peaks at 475 and 554 cm^{-1}) and carbon (D- and G-band at ~1350 and ~1600 cm^{-1}, respectively (Figure 9a). As shown in Figure 9b, the Raman image displays different colored pixels, red, blue, and green corresponding to the integrated band intensities of NCA, and D, G carbon bands of single spectrum, respectively. Figure 9c shows that the NCA spectral response, the intensity band ratio I_{475}/I_{554} and the peak FWHM are position dependent. These results evidence the spectral distortion due to the variation of the excited electronic states. Similar results obtained from mapping of $Li_{1-x}(Ni_yCo_zAl_{1-y-z})O_2$ maintained at different SOCs were explained in terms of a link between the variation of composition and the structural integrity at the single particle level [50].

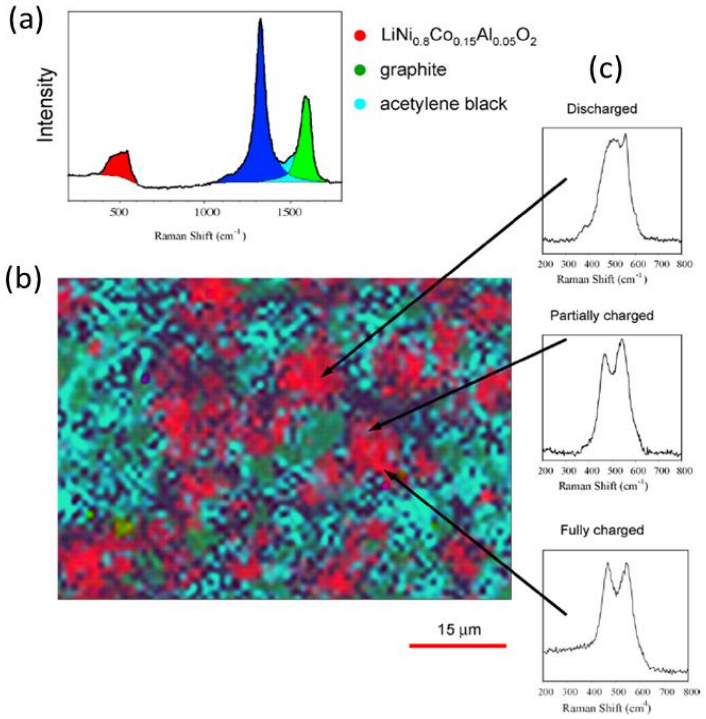

Figure 9. (a) Average Raman spectrum of the fresh composite $LiNi_{0.8}Co_{0.15}Al_{0.05}O_2$ electrode, (b) Raman image of the composite cathode where red, blue, and green pixels correspond to the integrated band intensities of E_g and A_{1g} modes of NCA, and D-, G-band of carbon of each spectrum, respectively; (c) Raman microscope spectra of three individual NCA particles. Reprinted by permission from Ref. [11].

3.2. Spinel-type compounds

3.2.1. $LiMn_2O_4$ (LMO)

Among the three-dimensional frameworks, spinel $LiMn_2O_4$, is an interesting cathode material as it is a low-cost material with low environmental impact. It generally exhibits reduced volume expansion upon lithium extraction/insertion reaction. $LiMn_2O_4$ grows in the cubic structure (*Fd*3*m* space group), in which cations occupy octahedral (Mn: 16*d*) and tetrahedral (Li: 8*a*) sites in the cubic close-packed array of oxygens occupying 32*e* Wyckoff positions. Extraction of Li ions from $Li_{1-x}Mn_2O_4$ ($0 < x < 1$) occurs with two voltage plateaus at ca. 3.95 and 4.15 V vs. Li^+/Li in between the $LiMn_2O_4/Li_{0.5}Mn_2O_4/\lambda$-$MnO_2$ end phases that correspond to the oxidation of Mn^{3+} to Mn^{4+} [80]. $Li_{1-x}Mn_2O_4$ is a stable phase: the removal of Li from $Li_{1-x}Mn_2O_4$ (oxidation process) occurs with a gradual decrease of the unit cell volume through a two-step redox reaction at the two voltage plateaus. However, the identification of the phases during Li extraction from $LiMn_2O_4$ to λ-MnO_2 has been debated in several publications involving two- or three-phase structural models [81–86].

A complete factor group analysis of the vibrational modes of the ideal AB_2O_4 spinel structure was given by White and DeAngelis [87] and revisited by Ammundsen et al. [88]. In the O_h^7 symmetry there are five Raman active modes represented by:

$$\Gamma_{LiMn_2O_4} = A_{1g} + E_g + 3T_{2g} \quad (3)$$

which decomposes in $A_{1g} + E_g + 2T_{2g}$ as internal modes and $1T_{2g}$ as an external (translational) mode. The experimental Raman spectrum displays 6 peaks distributed as follows: (i) the low-frequency peak at ca. 162 cm^{-1} is the $T_{2g}(1)$ translational mode that derives from the Li sublattice vibration, (ii) the E_g and $T_{2g}(2)$ modes are observed at 434 et 455 cm^{-1}, respectively, (iii) due to the presence of mixed valence state of Mn ($Mn^{3.5+}$) in $LiMn_2O_4$, the A_{1g} mode related to the Mn–O symmetric stretching mode is split into two components at 577 and 625 cm^{-1} attributed to the vibrations $\nu(Mn^{+IV}–O)$ and $\nu(Mn^{+III}–O)$, respectively, (iv) the high-frequency band at 654 cm^{-1} is the $T_{2g}(3)$ mode predominantly characterized by large oxygen displacements.

Investigations of the phase evolution of $LiMn_2O_4$ during charge–discharge process have been reported by several groups using *in situ* Raman spectroscopy [89–94]. The main spectral fingerprints of the spectra of $LiMn_2O_4$ and λ-MnO_2 consist in intense peaks at 593 and 628 cm^{-1}. Kanoh et al. [89] studied the electro-insertion of Li^+ in λ-MnO_2 using *in situ* Raman spectroscopy, and demonstrated that the logarithm of the intensity ratio $\log(I_{593}/I_{628})$ is an accurate measure of the variation of the lithium content, x, in $Li_{1-x}Mn_2O_4$ spinel lattice. In their early work, Huang and Frech [90] investigated the phase diagram of stoichiometric $Li_{1-x}Mn_2O_4$ and non-stoichiometry $Li_{1.1-x}Mn_2O_4$ cathode materials. Raman spectra of the former electrode ($0.1 < 1 - x < 1.0$) showed a single-phase followed by a two-phase process, and finally by another single-phase reaction, whereas the latter electrode displayed the presence of λ-MnO_2. Modifications of the vibrational properties of a single microparticle of $Li_{1-x}Mn_2O_4$ were monitored *in situ* via simultaneous Raman spectroscopy and cyclic voltammetry. In the potential range 4.021–4.118 V, a markedly asymmetric band centered at ca. 600 cm^{-1} are attributed to the T_2 and A_1 modes of the $Li_{0.5}Mn_2O_4$ (half-charged) phase, whereas two prominent bands located at 495 and 588 cm^{-1} are due to the $T_{2g}(2)$ and A_{1g} modes of λ-MnO_2 (full charged), respectively, for electrode voltage higher than 4.131 V [92]. Shi et al. [93] reported similar Raman experiments on $LiMn_2O_4$ single crystal microelectrode and showed that the SOC derived from optical data displays two well-defined steps up to fully oxidized material. Anzue et al. [93] studied the effect of the excited laser lines of 647.1 nm (1.97 eV), 514.5 nm (2.48 eV) and 457.9 nm (2.71 eV) on *in situ* Raman spectra of $Li_{1-x}Mn_2O_4$. They found a resonance enhancement effect for $x = 1$ (λ-MnO_2). This energy dependence attributed to the variation of the bandgap as a function of the Li content. Using a confocal Raman microscopy method, Slautin et al. [51] investigated the degradation paths in $LiMn_2O_4$ electrodes. Upon cycling, it is shown that the Mn_3O_4 phase is formed and dissolved that induces a local disturbance of the lithiation state.

Figure 10 shows the in-situ Raman spectra recorded using the 532 nm laser excitation line of $Li_{1-x}Mn_2O_4$ electrode during the charge at C/20 rate as a function of the electrode potential in the range 3.2–4.45 V vs. Li^+/Li [91]. The evolution of the frequency shift of Raman peaks that describes the $Li_{1-x}Mn_2O_4$ phase diagram in the composition range $0 \le x \le 0.88$ is presented in Figure 11. Three distinct single phases are identified from the spectral features during the charge process: (i) the phase of the initial compound $LiMn_2O_4$ (phase 1) is maintained up to $x = 0.10$, (ii) this phase coexists with an intermediate phase (phase 2) up to $x = 0.6$, (ii) above which a single intermediate phase (phase 2) is identified in a short range of composition $0.6 < x < 0.66$. (iii) a two-phase system between phase 2 and phase 3 is then observed in the range $0.7 \le x \le 0.8$, (iv) the single Li-poor phase (phase 3) is observed for $x > 0.80$. Note that the intermediate phase 2 has been previously reported from X-ray diffraction [86] and by Raman spectroscopy [88,91] analysis. Ammundsen et al. [88] identified this phase as an ordered structure $Li_{1-x}Mn_2O_4$ ($0.5 \le x \le 0.7$) with lower symmetry (space group F-43m, point group T_d^2), due to a distortion of the initial cubic lattice and vacancies in Li tetrahedral sites.

According to White and DeAngelis, the ordered cubic spinel (III) displays 12 Raman active modes represented by $\Gamma_{Li0.5Mn2O4} = 4A_1 + 3E + 6T_2$. It is worthy to make the following remarks: (i) using neutron and ex situ X-ray diffraction studies, the intermediate phase was only observed by Liu et al. [82] due to the difficulty to distinguish bi-phased domains at low C-rate (<C/10). On another hand, Raman spectroscopy is predominantly a weak penetrating probe, which investigates the delithiated phases formed at the surface of particles. (ii) It seems that the phase diagram in the 4-volt region is sensitive to the Li stoichiometry; as shown by *in situ* X-ray diffraction [95] lithium-deficient $Li_{0.99}Mn_2O_4$ and lithium-rich $Li_{1.04}Mn_{1.93}O_4$ show three cubic phases with the existence of two-phase domains due to the overlap of the adjacent phase.

Micro-Raman mapping was used to investigate the local structure of Ce-doped $LiMn_2O_4$ as shown in Figure 12a with the Raman spectra of Li–Mn–O components (Figure 12b). By probing the A_{1g} mode shift, spectral components observed in Figure 12a are as follows: (i) the largest area (blue regions) represents the pristine spinel (628 cm^{-1}), (ii) some spots originate from the monoclinic Li_2MnO_3 phase (616 cm^{-1}, white spots), (iii) a small fraction of distorted lattice spinel is shown by green spots (646 cm^{-1}) and (iv) a small fraction of signal comes from CeO_2 particles [96].

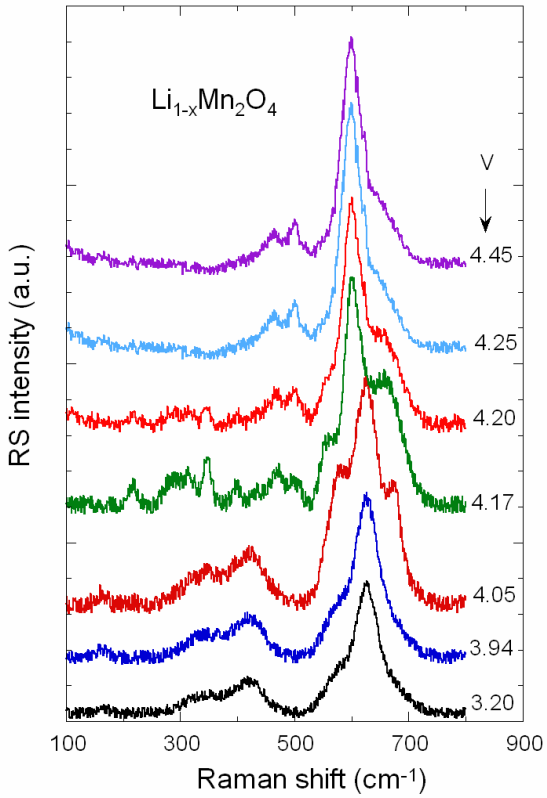

Figure 10. *In situ* Raman spectra of $Li_{1-x}Mn_2O_4$ electrode during the charge at C/20 rate as a function of the potential electrode in the range 3.2–4.45 V vs. Li^+/Li. Spectra were recorded using the 532 nm laser excitation line.

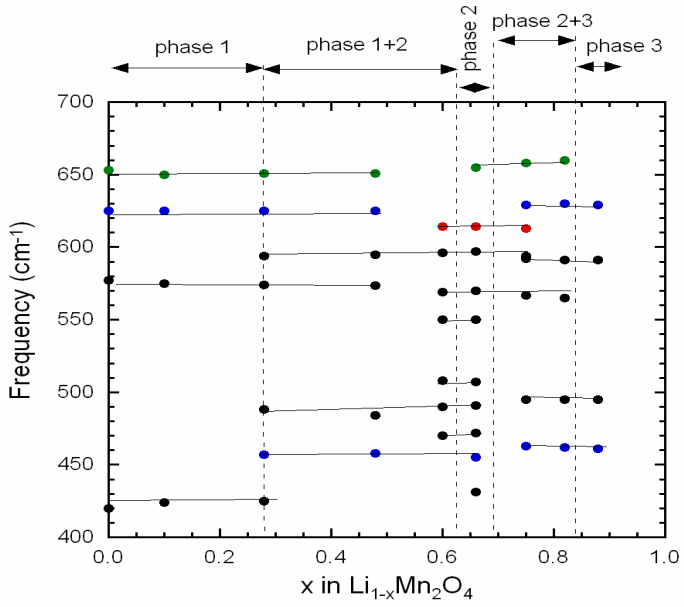

Figure 11. Evolution of the frequency shift of Raman peak describing the $Li_{1-x}Mn_2O_4$ phase diagram in the composition range $0 \leq x \leq 0.88$.

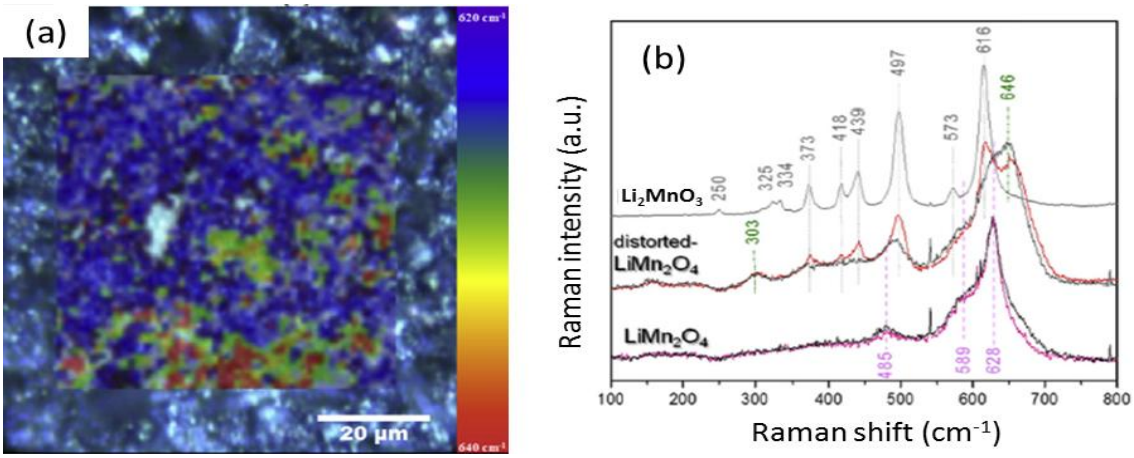

Figure 12. (a) *in situ* Raman mapping of Ce-doped $LiMn_2O_4$, (b) Raman spectra of Li-Mn–O components. Reprinted by permission from Ref. [96].

3.2.2. $LiNi_{0.5}Mn_{1.5}O_4$ (LNM)

$LiNi_{0.5}Mn_{1.5}O_4$ spinel (denoted LMN hereafter) is considered to be a promising high-voltage (4.7 V vs. Li^+/Li) cathode materials for powering hybrid electrical vehicles (HEVs) and plug-in hybrid electric vehicles (PHEVs). However, this material suffers from the presence of Jahn-Teller Mn^{3+} ions, cation ordering, and oxygen vacancies, which affect its high-rate performance. Recent investigations showed that the partial substitution of Ni and Mn by cations, such as Cr, Co, Fe, Nb, Mg, Zn, etc. [97–103] stabilizes the disordered LNM phase (*Fd*-3m space group) and eliminates the impurities of $LiNiO_x$, leading to electrochemical improvements. Typical Raman spectra of pristine and doped LNM electrodes are presented in Figure 13 with attribution of the spectral features [103].

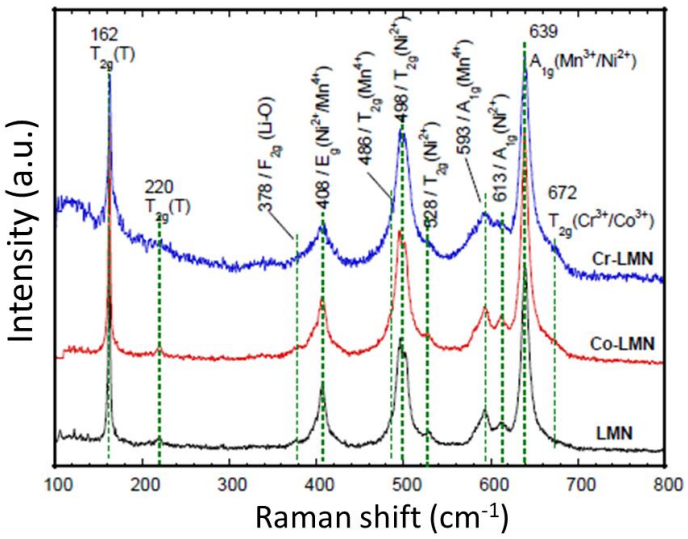

Figure 13. Raman spectra of as-made LNM electrodes. Reprinted by permission from Ref. [103].

The in-situ XRD studies on the phase evolution of LNM cathodes during cycling reveal that the doped materials have identical phase diagrams showing three cubic phases and the patterns reveal a decrease of the amount of Mn^{3+} Jahn-Teller ions leading to an increase of the rate capability [101]. In-situ Raman spectroscopy of doped $LiNi_{0.5}Mn_{1.5}O_4$ spinel cathodes was employed to investigate the valence state variations of nickel and manganese, as well as the local structure change during galvanostatic charge–discharge [102,103]. The early report of the in-situ Raman spectra of $LiNi_xMn_{2-x}O_4$ ($0 < x < 0.5$) thin films collected in the potential range 3.4–5.0 V vs. Li^+/Li showed a Raman band located at 540 cm^{-1} appearing at ~4.7 V, assigned to the Ni^{4+}–O bond. It was suggested that, upon cycling, the redox reactions $Ni^{2+/3+}$ and $Ni^{3+/4+}$ occurred in the potential range 4.4–4.7 V and 4.7–5.0 V, respectively [102].

Figure 14 shows the Raman spectra of Cr- and Co-doped samples collected between 3.5 and 4.9 V [103]. In the wavenumber range of 100–800 cm^{-1} the Raman spectra contain the bands of the pristine LNM with eleven features: (i) the bands at 162 and 220 cm^{-1} are attributed to the translation mode of molecular vibration, (ii) the 486, 593 and 639 cm^{-1} bands are assigned to the stretching mode of Mn–O bond, (iii) the vibration modes at 408, 498, 528 and 613 cm^{-1} originated from the Ni–O bond. In addition, a new band is introduced by the doping at 672 cm^{-1} and is attributed to A_{1g} mode of Cr^{3+}–O/Co^{3+}–O. Near the end of charge process at ca. 4.80 V, several new bands are detected among which (i) the T_{2g}(T) band at 170 cm^{-1} is attributed to the translation mode, and (ii) the T_{2g} band at 538 cm^{-1} is due to the presence of Ni^{4+}–O bond in the delithiated lattice. These Raman bands are clearly observed at $V \geq 4.78$ ($x \sim 0.32$) and $V \geq 4.82$ ($x \sim 0.28$) for Cr- and Co-doped LMN, respectively. The high-wavenumber band at 672 cm^{-1} assigned to Cr^{3+}–O/Co^{3+}–O vibration remains fixed during cycling, which proves that the valence state of Cr and Co ions is invariant [103].

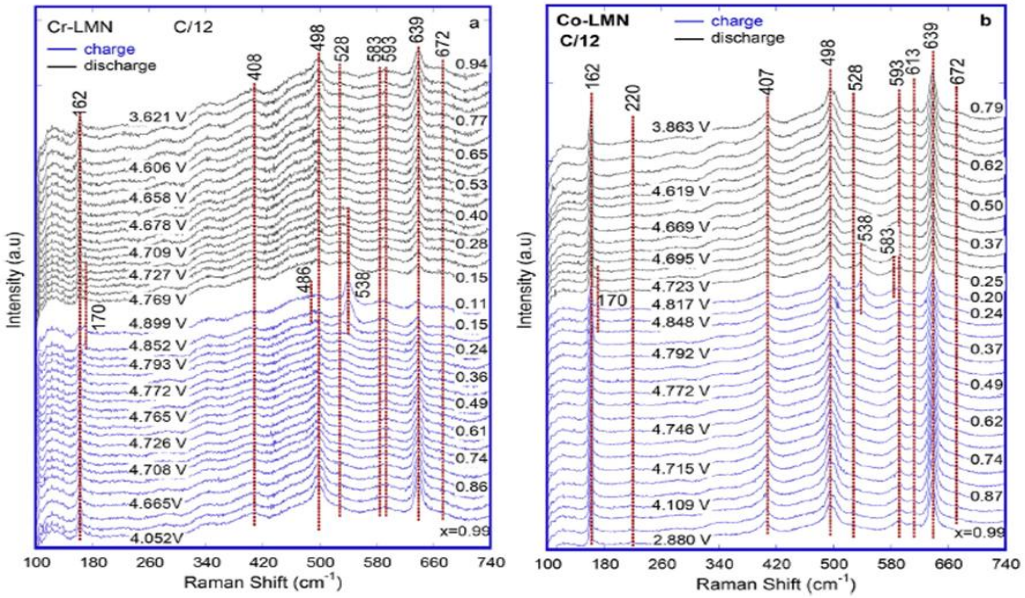

Figure 14. Evolution of *in situ* Raman spectra in one charge–discharge cycle at C/12 rate for (a) $LiMn_{1.45}Ni_{0.45}Cr_{0.1}O_4$ and (b) $LiMn_{1.45}Ni_{0.45}Co_{0.1}O_4$. Reprinted by permission from Ref. [103].

3.3. Vanadium pentoxide (V_2O_5)

V_2O_5 is an attractive electrode material which can accommodate 3 Li per mole of oxide to deliver a specific capacity of 450 mAh g^{-1} within the potential range 1.5–4.5 V vs. Li^+/Li [104]. Vanadium pentoxide, V_2O_5, with high-valent V^{5+} cations, are layered structures which consist of edge and corner-sharing VO_5 square pyramids attached by weak chemical bonds favourable to Li insertion process. The phase diagram of $Li_xV_2O_5$ is rather complex with reversible and irreversible phases across the composition $0 < x < 3$. Over the composition $0 \leq x \leq 3$, $Li_xV_2O_5$ undergoes the phase transitions with the corresponding potential plateaus $\alpha \rightarrow \varepsilon$, $\varepsilon \rightarrow \delta$ and $\delta \rightarrow \gamma$ at 3.4, 3.2 and 2.3, respectively. The γ-phase is irreversibly transformed into the ω-phase at the potential 2.05 V ($x > 2$). From XRD patterns, it was shown that, upon lithiation from α to to ε-phase, the lattice parameter, *a*, decreases continuously, while the lattice parameter *b* remains almost unchanged. *In situ* Raman spectra of Li intercalated V_2O_5 have been measured on crystal [19,30,105] and thin films [106,107] to characterize structural changes in $Li_xV_2O_5$ according to different C-rates, but also to study the abnormal stress modification upon phase transitions [107,108]. The first *in situ* Raman spectrometry studies of electrochemically lithiated and delithiated V_2O_5 materials were reported by Frech et al. [10,30,105]. Findings of Raman patterns of $Li_xV_2O_5$ electrodes are as follows: (i) a shift of the low-frequency B_{1g}/B_{3g} Raman peak (translational mode) from 144 to 154 cm^{-1}, (ii) a progressive intensity decay of the spectral response in the range 195–715 cm^{-1} attributed to the reduction of V^{5+} to V^{4+} generating negative charge carriers, (iii) the subsequent reduction of the optical-skin depth due to the metallic nature of the Li-intercalated V_2O_5 electrode, (iv) the disappearance of the vanadyl stretching mode at 996 cm^{-1} at electrode potential of ~3.27 V vs. Li^+/Li, replaced by a new peak at 983 cm^{-1} observed at ~3.40 V related to the coexistence of the α- and ε-$Li_xV_2O_5$ phases, (v) the new peak at 983 cm^{-1} shifts down to 972 cm^{-1} for further degree of Li

insertion corresponding to the ε-$Li_xV_2O_5$/δ-$Li_xV_2O_5$ two-phase system, (vi) finally, the γ-$Li_xV_2O_5$ phase is characterized by a peak at 975 cm^{-1} and the disappearance of the peaks at 196, 302, 484 and 700 cm^{-1} due to a loss of crystallinity in the γ-phase. Jung et al. [108] reported that the Raman patterns are not detected in the γ → ω phase transformation suggesting that the ω-phase has a quasi-amorphous structure. Studies of Li insertion in $Li_xV_2O_5$ film, suggested that the shift of the low-frequency peak from 144 to 154 cm^{-1} is due to the increase in the restoring force consequently to the tensile stress in the $Li_xV_2O_5$ film [109]. This assumption was confirmed by a combined approach (micro-Raman and optical stress sensor) correlating the Raman shift of B_{1g} + B_{3g} mixed modes with the more tensile stress as a function of the Li content in the $Li_xV_2O_5$ electrode [108]. The initial V_2O_5 orthorhombic symmetry (*Pmmn* space group) is kept upon Li intercalation in the $Li_xV_2O_5$ film ($0 \leq x \leq 0.94$) due to a solid-solution behavior leading to the typical Raman signature of the ε-$Li_{0.94}V_2O_5$ phase. During electrode charging, the local structure is completely recovered, the reason for the excellent electrochemical reversibility of V_2O_5 thinfilms prepared by atomic layer deposition (ALD).

The changes of the Raman spectra during the discharge process (lithiation) depend on the V_2O_5 synthesis technique [108]. In the works by the Pereira–Ramos's group [106,110–112] the Raman spectra differs for ALD samples, for rf-magnetron sputtering films and for sol-gel powders. Baddour-Hadjean et al. assumed that the decrease in the intensity of the low-frequency B_{1g}/B_{3g} Raman active mode located at 144 cm^{-1} reflects the structural disorder occurring upon V_2O_5 lithiation [113]. Therefore, the peak height I_{144} variation was correlated with the Li content in the $Li_xV_2O_5$ cathode and the dependence of the induced disorder during cycling with C-rates. Jung et al. [107] analyzed the charge rate dependent stress and structure changes in V_2O_5 electrode synthesized by ALD using an in-situ Raman micro-spectrometer equipped with a 532 green laser combined with a stress monitor. As shown in Figure 15, an exponential dependence of I_{144} on the degree of Li intercalation is observed in the composition range $0 < x < 0.2$. When the cathode is discharged at high C-rate (>C/4), the slope of ln(I_{144}) increases, which reveals an increase of the structural disorder in $Li_xV_2O_5$.

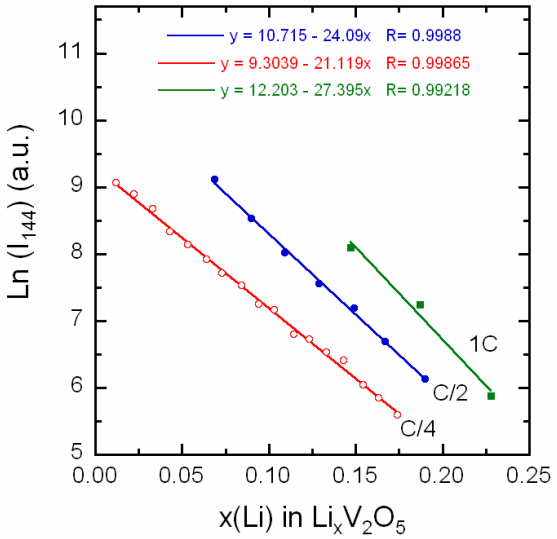

Figure 15. Plot of the logarithm of the peak height of the 144 cm^{-1} Raman band as a function of Li content in $Li_xV_2O_5$ (adapted from Ref. [107]).

3.4. Manganese dioxide (MnO_2)

Manganese dioxide, MnO_2 has been extensively studied as an active material for Leclanché dry cells, lithium-ion batteries and pseudocapacitors. The most popular phases used in energy-storage systems are γ-MnO_2 (pyrolusite/Ramsdellite intergrowth), α-MnO_2 (hollandite or cryptomelane phase) and δ-MnO_2 (layered birnessite phase). The crystallization in one of these different phases is determined by the synthesis conditions [114].

The charge storage mechanism (Li^+ ions incorporation) of a pseudocapacitive α-MnO_2 electrode was probed using in operando Raman spectroscopy. Raman spectra were obtained using a 514 nm excitation source and a confocal slit of 5 μm. the MnO_2 electrode was tested with different cations in the electrolytes (Li^+, Na^+ and K^+) in order to validate the best electrolyte of the pseudocapacitor [115]. Four major active Raman bands labelled ν_1 to ν_4 located at ca. 640, 577, 515 and 390 cm^{-1}, respectively, were considered for this purpose, since they describe the intrinsic vibration modes of pristine MnO_2. According to Julien et al. [116,117], the ν_1 band (620–650 cm^{-1}) is assigned to the symmetric stretching vibration of Mn–O bond in the MnO_6 octahedral environment; the ν_2 band (570–590 cm^{-1}) is assigned to the Mn–O vibration along the chains of the MnO_2 network, whereas the band at 390 cm^{-1} originates from the Mn–O bending vibrations. Based on the monoclinic structure (*C*2/*m* symmetry) of Li-intercalated MnO_2, the irreducible representations of the Raman active modes are classified as:

$$\Gamma_{LiMnO_2} = 10A_g + 8B_g \quad (4)$$

Figure 16 shows the in-situ Raman spectra evolution of MnO_2 film cycled within pseudocapacitive conditions in 2 mol L^{-1} $LiNO_3$ aqueous electrolyte between 0.7, 0 and 0.7 V vs. Ag/AgCl. Changes in the Raman spectrum are as follows. (i) At the beginning of the cycle (0.7 V), water molecules fill the interlayer spacing with Mn in the highest oxidation state (~Mn^{4+}). As the cathodic reaction proceeds (0.7 V to 0.0 V), the position of the ν_1 peak shows a red shift while the ν_2 band position underwent a blue shift. As pointed out by Julien et al. [118] the band shifts imply a reduction of the interlayer spacing upon the cathodic process due to the replacement of Li^+ ions for water molecules. (ii) At 0 V, the spectrum is close to that of $Li_{1.0}MnO_2$ [119]. While the band frequencies ν_1 (616 cm^{-1}), ν_2 (586 cm^{-1}) and ν_3 (480 cm^{-1}) match well with spectral features of $Li_{1.0}MnO_2$, the weak ν_4 is observed at 402 cm^{-1} instead of 420 cm^{-1}, which could be due the lower amount of incorporated Li^+ ions. (iii) The ν_1 and ν_2 bands become broadened due to the structural distortion induced by the increase of Mn^{3+} Jahn-Teller ions, (iv) the evolution of the peak intensity ratio $I(\nu_2)/I(\nu_1)$ (polarizability change) is attributed to the exchange of neutral H_2O by charged Li^+ cations and (v) during the cathodic process, the weak band ν_3 displays a doublet, while the ν_4 band shows reverse behavior [120].

Note that the reversible expansion and shrinkage in lattice spacing during charge transfer at manganese sites upon reduction/oxidation of MnO_2 demonstrated by the Raman spectroscopy is a direct proof that the pseudocapacitance involves intercalation or insertion of cations into the bulk of the oxide structure and is not limited to only the surface in contact with the electrolyte, as it was thought in the early stage of the study of the charge storage mechanism in this material.

The origin of high stability of the birnessite δ-MnO_2 pseudo-capacitive electrode synthesized by electroplating was elucidated using operando Raman spectroscopy at different states of charge/discharge. *In situ* spectra were collected using a green laser (λ = 514.5 nm) and a long

working distance of 50× objective lens. The electrochemical tests of the electrode were carried out galvanostatically between 0 and 1 V vs. Ag/AgCl at a 60 A g^{-1} current density in solution containing 1 mol L^{-1} Na_2SO_4 as electrolyte [121]. During charge/discharge cycling, three major Raman bands ν_1 (677 cm^{-1}), ν_2 (589 cm^{-1}) and ν_3 (507 cm^{-1}) show frequency shifts due to the structural evolution. For increasing applied potential 0.0 → 1.0 V (charge process) the ν_2 band at 589 cm^{-1} shifts down to 572 cm^{-1}, which corresponds to the expansion of the interplanar spacing due to the modification of the oxidation state of Mn^{4+} occurring for extraction of Na^+ ions and incorporation of water from the solution. During charge, the new peak ν_1 (677 cm^{-1}) is assigned to an intermediate Mn–O oxide state because of the coexistence of Mn^{4+} and Mn^{3+} cations. The reverse mechanism occurs during discharge (Na^+ ions insertion). Moreover, theoretical calculations also demonstrated that the incorporation of Na^+ into δ-MnO_2 is more energetically favorable than H^+ at all available sites of the interlayer space.

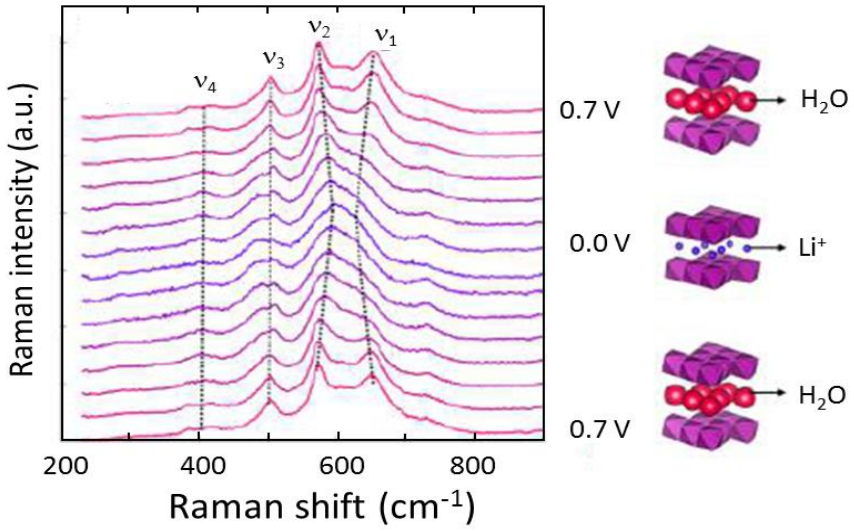

Figure 16. *In situ* Raman spectra evolution of MnO_2 film cycled in 2 mol L^{-1} $LiNO_3$ aqueous electrolyte between 0.7, 0 and 0.7 V vs. Ag/AgCl. Reprinted by permission from Ref. [120].

3.5. $LiFePO_4$ olivine

In the last decade, $LiFePO_4$ (LFP), member of the family of $AB^{II}XO_4$ olivine orthophosphates, has become an attractive positive electrode material for Li-ion batteries because their low cost and excellent thermal stability [122]. According to the group factor analysis of the LFP structure with *Pnma* space group (D_{2h}^{16} point group), the 36 Raman active modes at the centre of Brillouin zone are classified as:

$$\Gamma_{LiFePO_4} = 11A_g + 7B_{1g} + 11B_{2g} + 7B_{3g} \quad (5)$$

Raman spectrum of LFP includes: (i) the high-frequency bands in the region 908–1126 cm^{-1} that are stretching modes of P–O bonds, (ii) vibrations in the medium-frequency range between 487 and 691 cm^{-1} that are O–P–O bending internal modes of the PO_4^{3-} anion, (iii) external modes in the

low-frequency region between 175 and 335 cm^{-1} and (iv) the four peaks between 402 and 445 cm^{-1} correspond to the Li cage modes in octahedral coordination with O^{2-} anions [123]. Wu et al. [124] studied the evolution with x of *in situ* Raman spectra of Li_xFePO_4 samples (non-carbon coated) with different morphologies, i.e., nanoparticles and bulk particles, during galvanostatic charge/discharge process. The phase change from $LiFePO_4$ to $FePO_4$ is characterized by the shifts in the internal modes (stretching region), the appearance of peaks at 175 and 244 cm^{-1}, the intensity growth of external modes and the peak broadening of near 960 cm^{-1}. The symmetric stretch (ν_1 at 1102 cm^{-1}) is displaced to lower frequencies and splits in two bands at 1093 and 1091 cm^{-1}. Among the antisymmetric stretchs (ν_3), the peak at 1023 cm^{-1} disappears in the spectrum of $FePO_4$, while a red shift is observed for bands at 1011 and 978 cm^{-1}; the symmetric stretch (ν_1) blue-shifts from 953 to 975 cm^{-1}. Finally, a new peak at 908 cm^{-1} comes from the red shift of an asymmetry stretch. The largest LFP particles show incomplete delithiation, which could be due to the effect of anti-site defects on the surface preventing Li^+ ion motion in the 1D channels as evidenced by TEM experiments [125]. Siddique et al. [126] have combined two in operando techniques, micro-Raman spectroscopy and X-ray diffraction to study the $Li_{1-x}FePO_4$ phase change in samples with distinct length scales, i.e., particle level scale (≈1 μm) and macroscopic scale (≈several cm) using $LiPF_6$ in EC + DMC solution. In addition to the symmetric stretching mode (ν_1) of PO_4^{3-} anions, the Raman spectrum displays the characteristic bands from the electrolyte: (i) the peaks at 915 and 895 cm^{-1} are assigned to C–O stretchs of carbonate groups in non-solvated DMC and EC, respectively, which shift to 932 and 904 cm^{-1} in solvated solution, (ii) the peak at 714 cm^{-1} is attributed to the symmetric C=O ring deformation in EC, which moves to 720 cm^{-1} in solvated EC. In contrast with ex situ measurements [127], the in-situ Raman of the delithiated LFP electrode was able to display conclusive interpretation of the peak profile at 950 cm^{-1} peak nor new bands in the range 910–1050 cm^{-1}. In particular, from the spectroscopic study of ion-solvent interactions, it was shown that the intensity of the C–O stretch is a linear function of the salt concentration that leads a blue shift in solvated products. The relative intensity of solvation, I_r, is expressed as [128]:

$$I_r = I_s/(I_s + I_n) \tag{6}$$

where I_s is the intensity of solvated molecule and I_n the intensity of bulk non-solvated molecule. Therefore, the variation of the Li^+ concentration at the LFP particle surface, C_{Li}, depends on the electrode potential and C-rate. C_{Li} decreases at the beginning of the charge and reached a minimum for the potential of 3.45 V (potential plateau), then C_{Li} increases till the charge at 4.0 V.

3.6. $Li_3V_2(PO_4)_3$ (LVP)

Polyphosphate material such as α-$Li_3V_2(PO_4)_3$ (LVP) has a complex three-dimensional network with a monoclinic structure that provides mobility for three Li^+ ions, providing a high specific capacity of 197 mAh g^{-1}. According to the group factor analysis of the LVP structure with $P2_1/n$ space group (C_{2h} point group), there are 120 Raman active modes at the centre of Brillouin zone, which are classified as:

$$\Gamma_{\alpha\text{-}Li_3V_2(PO_4)_3} = 60A_g + 60B_g \tag{7}$$

Only 19 vibrational modes are observed in the unpolarized Raman spectrum located at ca. 1078, 1059, 1030, 1009, 975, 652, 604, 560, 505, 454, 430, 375, 349, 290, 255, 224, 169, 134 and

118 cm^{-1}. Burba and Frech [129] studied the vibration spectra of electrochemically delithiated $Li_3V_2(PO_4)_3$ powders ($0 \leq x \leq 3$) and reported the high sensitivity of the $(PO_4)^{3-}$ modes with extraction of Li^+ ions and change of the vanadium oxidation state. After the first discharge process, Yin et al. [130] found the $(PO_4)^{3-}$ band broadening that is assigned to some local disorder in the relithiated lattice. The thermal phase stability of α-$Li_3V_2(PO_4)_3$ was investigated by *in situ* Raman spectroscopy by varying the irradiation power intensity from 5 to ~600 kW cm^{-2} (using a 1.3 μm spot diameter in air). The increase of temperature resulted in phase transitions in the sequence [8]:

$$\alpha\text{-}Li_3V_2(PO_4)_3 \rightarrow \beta \rightarrow \gamma \rightarrow \alpha\text{-}LiVOPO_4 \quad (8)$$

where the α-$LiVOPO_4$ material is the oxidation phase under air atmosphere.

3.7. β-$AgVO_3$ (SVO)

Silver vanadium oxide (SVO) has an important technological application in medical power sources as cathode material of lithium batteries for implantable cardio-pacemakers and defibrillators [131]. The structural changes and of Li inserted β-$AgVO_3$ nanoparticle were studied by *in situ* Raman spectroscopy using the blue excitation line (λ = 488 nm) combined with atomistic simulation to determine the lithium migration pathways [132]. Upon Li insertion, the reduction sites in the β-$AgVO_3$ lattice can be divided into three steps that correspond to the potential plateau in the discharge profile: (i) the most favorable reduction on sites V1/V4 occurs at higher potential 3.55–3.05 V, (ii) Ag2/Ag3 are reduced and substituted at medium potential 3.05–2.55 V and (iii) finally, Li^+ ion reduces V2/V3/Ag4 and further reduces V1/V4 in the potential range 2.55–1.75 V vs. Li^+/Li. In the first step, in which vanadium is reduced from V^{5+} to V^{4+}, the intensities of Raman peaks at 266, 530, 772, 808, 847 and 886 cm^{-1} are enhanced at 3.35 V and are further weakened at 3.05 V; the stretching vibration at 513 cm^{-1} of V–O bonds in pyramids exhibits a large blue shift to 530 cm^{-1}, while the asymmetric bending mode of $(VO_4)^{3-}$ pyramids at 278 cm^{-1} has a red-shift to 266 cm^{-1} related to the distortion of V1/V4 pyramids upon Li introduction in the host lattice. In the second step, the Raman spectrum becomes strongly attenuated due to the loss of resonance and to the increase of electrical conductivity that reduces the optical-skin depth. However, a blue shift of the Raman band at 807 cm^{-1} (to 811 cm^{-1}) due to the shortened V–O bond is observable. In the third step, no significant modification of the Raman features is detected in the potential range 2.55–2.05 V, while the band at 771 cm^{-1} shifts to 775 cm^{-1} between 1.85 and 1.75 V and the peak at 756 cm^{-1} splits into two components at 750 and 761 cm^{-1}. Moreover, the reduction of vanadium at the V1/V4 site occurring at 1.95 V is characterized by the spit of the band at 730 cm^{-1} in two well-resolved peaks at 723 and 734 cm^{-1}. These changes of the vibrational modes indicate a significant lattice distortion of β-$AgVO_3$ with Li insertion.

4. Negative electrodes

4.1. Carbonaceous materials

Numerous works prior 1998 have been devoted to the studies of local structure of carbonaceous materials used as negative (anodes) materials, for Li-ion batteries. The term carbonaceous include various forms of carbon materials from highly disordered networks (turbostratic graphite, glassy

carbons), to defect-free well crystallized crystals, i.e., highly oriented pyrolytic graphite (HOPG) characterized by its L_c and L_a parameters indicating dimensions perpendicular and parallel to the basal plane. A relation that is a measure of the structural order in the graphene sheets of carbonaceous materials has been established between the correlation length L_a (expressed in nm) and the derived spectral parameter, i.e., intensity ratio of Raman carbon-like bands $I(D)/I(G)$ [133]:

$$L_a = \frac{4.382}{I(D)/I(G)} \tag{9}$$

In this section, we will not expose in detail the results of *in situ* Raman but will only give some hints about the latest research.

4.1.1. Graphite intercalation compounds (GICs)

The layered structure of graphite consists of regular stacked graphene sheets arranged in hexagonal AB stacking sequence of $P6_3/mmc$ space group (D_{2h}^4 point group), of which the factor group analysis gives rise to two Raman active modes for $\boldsymbol{q} = 0$:

$$\Gamma_{\text{graphite}} = 2E_{2g} \tag{10}$$

The spectrum of graphite exhibits a low-frequency prominent peak E_{2g1} mode at 42 cm^{-1} (rigid-layer shear mode) that originates from the in-plane sliding of graphene sheets, and the predominant peak at 1580 cm^{-1} attributed to the E_{2g2} mode (in-plane C–C stretching mode) that is usually termed as G band. An additional Raman band at ~1350 cm^{-1} (D band) appears for polycrystalline graphites and non-graphitic carbons, which is the A_{1g} breathing mode activated by defects and grain boundaries. Overtone bands are also observed at ~2670 cm^{-1} (2D) and ~3250 cm^{-1} (2G) [134].

Since the early work of the Japanese's group [135], the changes in the local structure of graphite intercalation compounds (GIC) have been widely studied by *in situ* Raman spectroscopy [25,34,44,136–147]. At the open circuit potential (ca. 3.0 V vs. Li^+/Li), the Raman spectrum exhibits three bands in the region between 1000–3000 cm^{-1}: a weak D-band, a predominant G-band and a weak 2D-band. The staging process of Li intercalation into HOPG and natural graphite was first reported by Inaba et al. [135]. Using *in situ* Raman spectroscopy, they observed that Li intercalation into graphite proceeds via a series of staged GICs phases, noted by a stage index, *n*, which represents the number of graphene sheets separating the intercalated layers. It is claimed that Raman spectral changes are correlated with the potential plateaus recorded on the charging reaction as follows: a phase transition from dilute stage-1 to stage-4 followed by the stage-2' (LiC_{18}) → stage-2 (LiC_{12}) and stage-2 (LiC_{12}) → stage-1 (golden LiC_6) transitions. This model will be modified in further investigations of Lonza KS-44 and KS-6 graphite materials [136]. Panitz et al. [44] presented *in situ* Raman patterns and imaging of electrode made of TIMREX SFG 44 synthetic graphite with PVdF binder, which reveal a new band at ca. 1850 cm^{-1} at potential negative to 0.18 V vs. Li^+/Li assigned to the complex between Li ions and decomposition of the aprotic solution. This electrolyte/graphite interaction was later reconsidered by Novák et al. [137] in terms of SEI. The so-called dilute stage-1 phase of GICs was deeply studied on KS-44 carbon particles (8–50 μm in diameter) embedded in heat-treated Ni foils [138]. Kostecki and McLarnon [139] investigated the structural degradation of graphite electrodes by portraying the graphite D/G band ratio of the anode via a 50 μm × 75 μm cross-section Raman image.

During lithiation (discharge process from OCV (ca. 3.0 V) to 0.05 V), modifications of the first- and second-order Raman bands may be classified into four steps: (i) in the potential range 3.0–0.6 V, the D-band intensity vanishes, (ii) a blue-shift of the G-band from 1580 cm^{-1} to 1590 cm^{-1} occurs at ~0.19 V along with a weakening of the 2D(1) band intensity due to the formation of dilute stage-1, (iii) in the potential window 0.19–0.10 V, the G-band splits into the E_{2g2}(i) (1575 cm^{-1}) and E_{2g2}(b) (1601 cm^{-1}) bands, accompanied by a major red-shift of the 2D(2) band due to the formation of stage-2 and stage-1 and (iv) finally, a gradual loss of all distinct Raman peaks occurs below 0.10 V vs. Li^+/Li with the appearance of a weak band located at ca. 1370 cm^{-1}. The formation of highly conductive GIC at low-stage number is at the origin of the loss of all Raman features [148]. Note that the formation of the G-band doublet E_{2g2}(i) (1578 cm^{-1}) and E_{2g2}(b) (1600 cm^{-1}) is also observed in the case of the electrochemical intercalation of tetraethylammonium (Et_4N^+) and tetrafluoroborate (BF_4^-) into microcrystalline graphite [149]. The use of propylene carbonate (PC) provokes graphite exfoliation characterized by a new Raman band (E-band) at high wavenumbers of 1609 cm^{-1} between 0.9 and 0.005 V [144].

In the reverse reaction (lithium de-intercalation) four stages can be also considered: (i) a broad G-band at 1592 cm^{-1} and the weak band at 1370 cm^{-1} recurs at ca. 0.14 V, (ii) the E_{2g2}(b) band of the stage-2 GIC is formed at ca. 0.15 V from the blue-shift of the G-band from 1592 to 1598 cm^{-1}, (ii) both the G band doublet, E_{2g2}(i) (1573 cm^{-1}) and E_{2g2}(b) (1601 cm^{-1}) and the 2D(2) band reappear in the potential range 0.17–0.22 V and (iv) the sharp singlet G-band at 1586 cm^{-1} and the 2D(1) band are reformed coming to the delithiated structure between ca. 0.3–1.5 V. Note that the doublet E_{2g2}(i), E_{2g2}(b) is associated respectively with carbon vibrations in interior graphite layers and in-bounding graphite layers adjacent to the intercalate planes. This splitting is attributed to changes in symmetry at the boundary layer and to the change in electronic states upon Li^+ ion intercalation at stage $n > 2$. When intercalated graphite appears as stage-1 and -2, the E_{2g2}(i) band vanishes because of the absence of graphite interior layer. By taking into consideration the intensity ratio of the E_{2g} doublet (R), Solin has proposed a quantitative measure of the intercalation stage index, n, by the following equation [150]:

$$R = \frac{I_i}{I_b} = \frac{\sigma_i}{\sigma_b}\frac{n-2}{2} \qquad (n > 2) \tag{11}$$

where I_i and I_b are the intensities of the interior E_{2g2}(i) and bounding E_{2g2}(b) layer modes, respectively, and σ_i/σ_b is a stage-independent ratio of the Raman scattering cross-section from the interior and bounding layers, equal to 1 for lithium intercalation.

Typical *in situ* Raman spectro-electrochemical measurements of graphite electrode is presented in Figure 17, where spectral features were taken on different points that show the inhomogeneity of the particle distribution in the electrode [143]. Detailed real-time Raman spectra from a single KS-44 graphite microflake electrode determined that the transition between dilute stage-1 and stage-4 of lithiated GIC occurs in the potential range 0.174–0.215 V vs Li^+/Li [141]. Graphite surface disorder was detected by the variation in electrode potential of the appearance of the G-band doublet associated to the formation of stage-4 GIC [143]. During lithium intercalation in hydrogen-rich amorphous carbon, lithium-carbon interaction leads to an increase of I_G/I_D and formation of Li–C bands at ~480 and ~700 cm^{-1} [151]. Raman imaging of synthetic graphite LF-18D particles with an average particle diameter of 22 μm (Chuetsu Graphite Works Co.) showed that the Li does not intercalate in a homogeneous manner; it varies with the article morphology and local

conditions [142]. *In situ* Raman experiments evidenced the intercalation effect of both large cation (EMI^+) and anion ($TFSI^-$) in KS44 microcrystalline graphite and PICACTIF activated carbon. Intercalation is detrimental for graphite with an increased I_D/I_G ratio, while possible intercalation of activated carbon upon cycling is evidenced by the blue-shift of the D-band [146]. The surface region of graphitic negative electrode (microcrystalline graphite) was examined by *in situ* real-time Raman measurements under potential control during Li^+-ion insertion and extraction [33]. A special attention was paid to the double resonance 2D-band that shifts from 2681 to 2611 cm^{-1}. The change of the electronic structure of the intercalated compound and the C–C bonding of stage 3 and 4 was evidenced by the band shape transformation into a single Lorentzian in the potential range 0.24–0.15 V vs. Li^+/Li. It was concluded that the Daumas–Hérold model can be applied, where the graphene sheets are flexible and deform around Li intercalated domains.

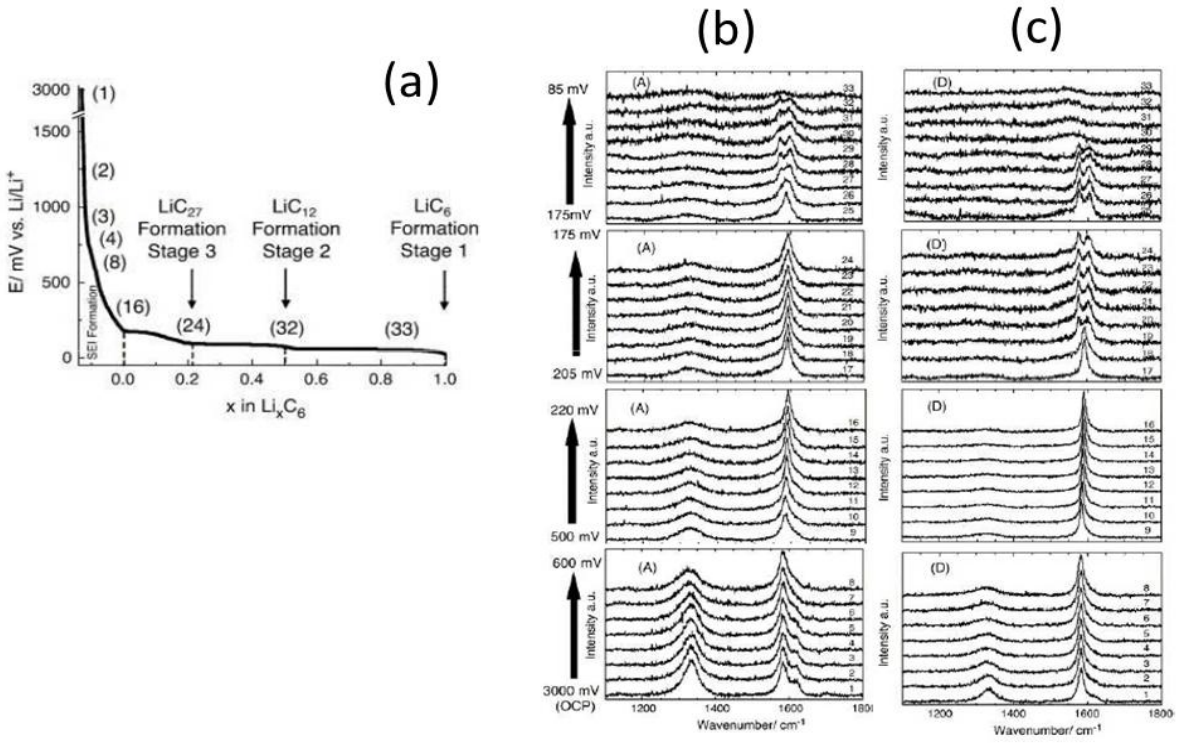

Figure 17. Typical *in situ* Raman spectro-electrochemical measurements of graphite electrode. (a) Potential profile during the lithiation of graphite showing the staged phase. (b and c) Spectral features as a function of the electrode potential taken on different points that show the inhomogeneity of the particle distribution in the electrode. Reprinted by permission from Ref. [143].

In situ Raman spectro-electrochemical measurements were also carried out to study the degradation of edge-plane graphite negative-electrodes [152], the SEI formation [153], the influence of the salt in the electrolyte solution on the structural degradation of graphite [154], the surface evolution of a single graphite particle with ethylene carbonate/dimethyl carbonate [155], the behavior of graphite electrodes in electrolyte solution containing fluorinated phosphoric esters [25], the decrease in the surface crystallinity of graphite negative-electrodes at high potentials in $LiPF_6$-

based electrolyte solution [156], the correlations of concentration changes of the electrolyte salt with the surface state of a HOPG graphite electrode, the Li^+ ion intercalation and deintercalation behaviors of graphitized carbon nanospheres [157] and the structure of heat-treated graphene nanoflake-based anodes [158].

4.1.2. Li insertion in other carbonaceous materials

By contrast to graphite, carbonaceous materials with non-graphitic structure exhibit poor galvanostatic responses with slopping potential profiles that originate from disorder. Coke, carbon black and glassy carbon (GC) deliver low-specific capacity, i.e., 223 mAh g^{-1} for GC against 372 mAh g^{-1} for graphite. The spectral modifications of the Raman E_{2g2} band of mesocarbon microbeads (MCMBs) annealed at 2800 ℃ presents a Li insertion mechanism similar to that of graphite with formation of staged phases [159]. Totir and Scherson [160] investigated the electrochemical lithium intercalation of embedded KS-44 graphite and MCF28 carbon microfibers and reported spectral patterns in good agreement with similar materials. The graphene oxide (GO) and reduced graphene oxide (rGO) obtained by scanning the cell potential from 0 to −1 V vs. SCE in an aqueous electrolyte were characterized by *in situ* Raman spectro-electrochemical study, which showed a clear shift of the G-band from 1610 to 1585 cm^{-1} for GO and rGO, respectively [161]. *In situ* Raman and nuclear magnetic resonance measurements were performed to study the trapped Li ions in the SEI of rGO [162]. It is shown that the graphitic G-band weakens and vanishes fast at potential >0.3 V without staged GIC and suggested that the monolithic defective sites are randomly accommodated by Li^+ ions, which cover the rGO surface and cause the G-band disappearance.

4.2. Lithium titanate $Li_4Ti_5O_{12}$ (LTO)

$Li_4Ti_5O_{12}$ (LTO) is an anode material being a zero-strain network with high thermal stability. It crystallizes in the cubic structure with *Fd*3*m* space group (O_h^7 point group) and can be expressed as $Li[Li_{1/3}Ti_{5/3}]O_4$ in the spinel notation; thus, the Raman-allowed phonon peaks are represented by species in Eq 3, while factor group analysis predicts 4 Raman-active modes for the lithiated phase $Li_2[Li_{1/3}Ti_{5/3}]O_4$ at $\boldsymbol{q} = 0$:

$$\Gamma = A_{1g} + E_g + 2T_g \tag{12}$$

The Raman spectrum of the pristine material exhibits three intense Raman bands centered at 671, 430 and 232 cm^{-1} along with two weak Raman peaks at 347 and 271 cm^{-1}. The vibration at 671 cm^{-1} (A_{1g} mode) is ascribed to the symmetric Ti–O stretch of TiO_6 octahedra, while the peak at 430 cm^{-1} (E_g mode) originate from the asymmetric Li–O stretch of LiO_4 tetrahedra and the 232 cm^{-1} band (T_g mode) from δ(Ti–O). The Raman peak at 232 cm^{-1} and other weak bands are assigned as T_{2g} mode [163]. During discharge, the lithiated $Li_{1+x}[Li_{1/3}Ti_{5/3}]O_4$ electrode can accommodate $x \approx 0.94$ Li with a CV curve showing a very wide potential plateau around 1.55 V vs. Li^+/Li. Insertion of Li^+ ions in octahedral 16*c* empty sites of the $Li_{1+x}[Li_{1/3}Ti_{5/3}]O_4$ framework and the reduction of Ti ions in TiO_6 octahedra provoke a gradual blue shift of Raman bands at 430 and 232 cm^{-1}, while the high-wavenumber peak at 671 cm^{-1} is maintained [164]. *In situ* Raman studies show that, at the end of the discharge, the spinel transforms in rock-salt lattice and, as the electronic conductivity increases

considerably due to the presence of Ti^{4+} and Ti^{3+} ions, the Raman line intensities gradually weaken with x and finally disappear at $x \approx 0.94$ due to the decrease of the optical-skin depth [165].

4.3. Titanium dioxide TiO_2

TiO_2 has been exhaustively investigated due to its attractive properties; it is low cost, thermally stable, environmentally safe, etc., and it is considered as a promising candidate for use in Li-ion batteries. TiO_2 exists in different polymorphic forms: anatase, rutile, brookite, TiO_2-B (bronze), TiO_2-R (ramsdellite), TiO_2-H (hollandite), etc. [166]. It appears that the potential profile of the Li//TiO_2 couple is strongly influenced by the structure; as an example, the working voltage of Li//anatase TiO_2 cell is higher than that of Li//rutile TiO_2 cell. Anatase TiO_2 (tetragonal structure, space group $I4_1/amd$, D_{4h}^{19} point group) can accommodate reversibly $x \approx 0.5$ Li that converts $Li_{0.5}TiO_2$ to orthorhombic phase (space group *Imma*, D_{2h}^{28} point group) [167]. Only nanocrystalline TiO_2 particles (<7 nm in size) are able to host $x \approx 1$ Li [168]. The lattice dynamics of pristine anatase TiO_2 has been subject to numerous works (see [29] and Refs. herein). Its first-order Raman analysis gives rise to 6 active vibrations at $\boldsymbol{q} = 0$:

$$\Gamma_{TiO_2} = A_{1g} + 3E_g + 2B_{1g} \tag{13}$$

which have been experimentally observed at 635, 515, 395, 195 and 142 cm^{-1} [169]. The symmetry change from D_{4h}^{14} to D_{2h}^{28} induced by elongated equatorial Ti–O bonds in $Li_{0.5}TiO_2$ produces 9 Raman active modes represented by:

$$\Gamma_{Li_{0.5}TiO_2} = 3A_g + 3B_{2g} + 3B_{3g} \tag{14}$$

where B_{2g} and B_{3g} modes come from the splitting of the E_g mode. Non-stoichiometry and phonon confinement in nanoparticles (>10 nm in size) produce a blue shift and a broadening of the lowest-frequency E_g vibration. Several studies reported *in situ* Raman spectro-electrochemistry of Li-inserted anatase TiO_2 [170–177]. Dinh et al. [170] combined *in situ* Raman and *in situ* transmittance spectra of electrochromic TiO_2 anatase thin films and demonstrated that the colored film exhibit five characteristic bands at 629, 531, 316, 224 and 176 cm^{-1}. Hardwick et al. [173] studied three nanosized TiO_2 anatase powders (80, 15 and 8 nm in size) and, using *in situ* Raman microscopy, followed the increase in electrical conductivity as lithiation proceeds, with a marked band intensity decrease for $x > 0.3$ in Li_xTiO_2. *In situ* Raman spectro-electrochemistry was a powerful tool to detect the contamination of anatase TiO_2 in the TiO_2(B) and TiO_2(rutile) polymorphs during Li^+ insertion/deinsertion [176]. *In situ* Raman spectro-electrochemistry showed that structural modifications during Li insertion in anatase TiO_2 nanoparticles can be understood by a mechanism of Li-poor tetragonal → orthorhombic → Li-rich tetragonal double phase transformation. For $Li_{0.09}TiO_2$ (at 1.75 V electrode potential), a blue-shift of the band at 142 cm^{-1} is observed ($\Delta\nu$ = 5 cm^{-1}) followed by the two-phase process characterized by the occurrence of two bands at 165 and 177 cm^{-1} that corresponds to the potential plateau at 1.4 V. The additional Raman peaks associated with the end-composition $Li_{0.5}TiO_2$ are recorded at 625, 555, 528, 355, 339, and 315 cm^{-1} [175].

4.4. Silicon

Silicon is an attractive anode material because of its low cost, its large specific capacity, i.e., 4200 mAh g^{-1} when lithiated to $Li_{4.4}Si$ (or $Li_{22}Si_5$), and its relatively low redox potential, i.e., 0.3–0.4 V above Li^+/Li [178]. However, the electrochemical performance of Li–Si alloys degrades due to the large volume expansion, i.e., 420% from Si to $Li_{4.4}Si$. During discharge the Li–Si alloy is formed and subsequently a transition from crystalline (c-Si) to amorphous (a-Si) silicon occurs. In this context, few researchers have studied the phase transformation using *in situ* Raman microscopy [179–183]. One of the earlier *in situ* Raman investigation of silicon anode was conducted by Holzapfel et al. [184]. Unlithiated Si material exhibits the typical first-order ($\boldsymbol{q}$ = 0) Raman peak at 520 cm^{-1} (optical phonon) of the crystalline phase that significantly decreases at potential below 0.88 V upon Li alloying. For further lithiation, the Si peak vanishes totally and a broad band grows at ca. 480 cm^{-1} when the discharge reaches 0.09 V, which could indicate the growth of an amorphous Li_xSi phase [179]. Nanda et al. [180] characterized the surface of the Si/C composite anode at a microscopic level and monitored the alloying/dealloying behavior of Si/C with Li, using *in situ* Raman microscopy study. As shown in the Raman spectra of silicon as a function of the first discharge between 2.0 and 0.45 V (Figure 18), the Raman peak of Si peak does not change (discharged at a current density of 90 μA cm^{-2}), while at 0.2 V the signal substantially decreases and disappears below 0.1 V due to the conversion of the crystalline Si into an alloyed Li–Si phase.

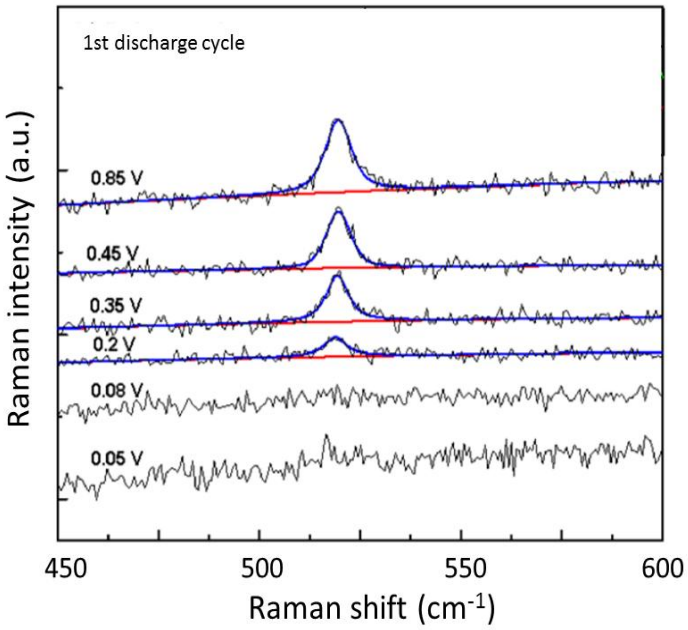

Figure 18. *In situ* Raman spectra of a Li//Si electrode discharged at a current density of 90 μA cm^{-2}. Reprinted by permission from Ref. [180].

Long et al. [185] examined the effects of p-type (boron) and n-type (phosphorus) dopants on the lithiation of crystalline Si. The transition to amorphous Si associated with the Li insertion was monitored by *in situ* Raman spectroscopy. A plot of the height of phonon peak shows that the n-type Si exhibits a phonon decay at potential of 0.09 V, against 0.68 V for the p-type Si. This effect is

explained in terms of energy states available to the electron associated with the Li^+ ion. The lithiation of silicon decorated by plasmonic metals, i.e., Ag and Au, was characterized by *in situ* Raman microscopy and Raman mapping on a section of 20 × 30 μm^2 using a laser wavelength of 532 nm [186]. The structural evolution, the internal strain and stress in the lithiated and delithiated Si nanoparticles were monitored by both *in situ* X-ray diffraction and in operando Raman spectroscopy [182,187]. Upon the formation of Li–Si alloys, the drop of the phonon intensity results first from the amorphization of the c-Si framework and secondly from the decrease of the optical-skin depth. There are no changes of peak position during the first discharge, while a blue shift occurs during delithiation. In contrast, the upshift that originates from compressive stress is followed by the downshift due to tensile stress during the second cycle and so forth. From the experimental Raman shifts, one can estimate the magnitude of the stress using the relation [182]:

$$\sigma = -230(\omega_s - \omega_0) \quad (15)$$

where ω_0 and ω_s are the wavenumbers for the relaxed and of the stressed particles, respectively. Yang et al. [188] experienced the lithiation behavior of Cu-nanowire/Si nano-particle composite anodes using *in situ* micro-Raman mapping, showing that the Li–Si reaction does not occur in a homogeneous manner due to disconnected active particles. Recently, Sakaguchi et al. strenuously determine silicon anode properties [189–191]. The deterioration mechanism of Si anode was analyzed using Raman mapping of Li–Si alloying and dealloying reactions [189]. Evolution of the Raman shift of the 520 cm^{-1} line of phosphorous-doped Si revealed that doping monitored the Li–Si alloying reaction and the formation of the c-$Li_{15}Si_4$ phase [190].

4.5. Other anode materials

4.5.1. Antimony

The active researches of high-performance anode materials have motivated the consideration of metal-containing compounds in the form of intermetallics such as Sb, InSb, Cu_2Sb, AlSb, etc. that make alloys upon lithiation [192]. Antimony is capable of 3Li uptake forming an alloy with a theoretical specific capacity of 660 mAh g^{-1} based on the Li_3Sb reaction [193]. The lithium alloying of carbon-coated antimony microparticles synthesized by a one-pot sol-gel auto-combustion route was analyzed by *in situ* Raman spectroscopy using a red laser-line (λ = 632.8 nm) as excitation source [194].

Using *in situ* Raman spectro-electrochemistry in the potential between 1.5 and 0.02 V, a comparison with commercially available Sb nanoparticles of same size (ca. 5–50 μm) shows a superiority of sol-gel prepared Sb (Figure 19). The Raman spectrum exhibits the signal due to D- and G-band of the disordered carbon coating and the phonons of antimony at 150 cm^{-1} (A_{1g} mode) and 112 cm^{-1} (E_g mode), which is sensitive to the confinement and strain of particles. During lithiation, the Raman spectrum of Sb is maintained until ~0.9 V vs. Li^+/Li and then the intensity of phonon vibrations decreases until smearing out at 0.02 V. Some degree of long range ordering is recovered upon delithiation to 1.5 V with the reemergence of the A_{1g} peak at 152 cm^{-1}.

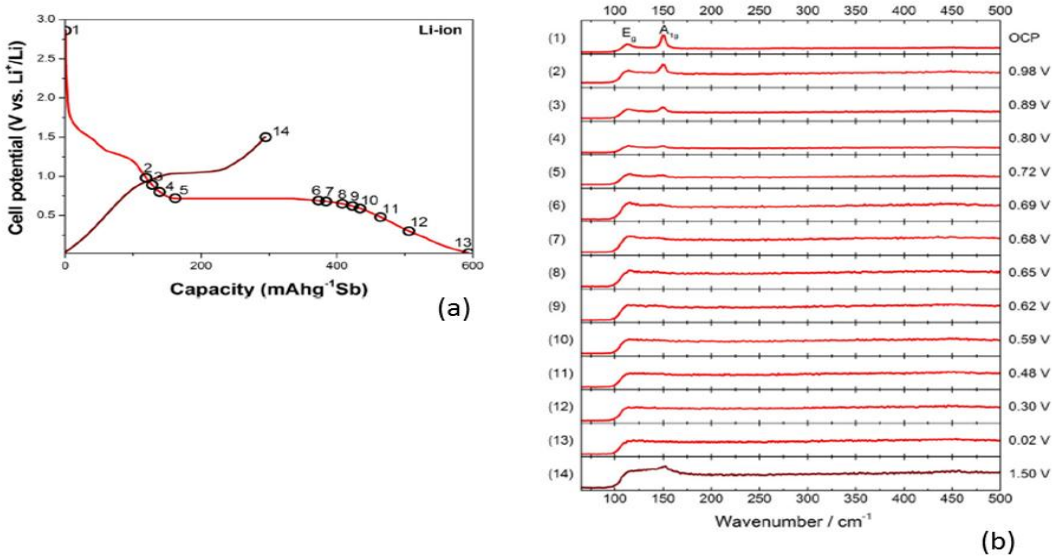

Figure 19. (a) Discharge–charge profile of the Li_xSb anode. (b) *In situ* Raman spectra collected in the potential between OCV and 0.02 V vs. Li^+/Li. Reprinted by permission from Ref. [194].

4.5.2. ZnM_2O_4 (M = Mn, Fe)

Among the ternary Zn-based oxides, the spinel $ZnMn_2O_4$ material reacts with lithium with both conversion and alloying process, which results in a specific capacity 1024 mAh g^{-1}. *In situ* Raman spectra of mesoporous $ZnMn_2O_4$ microspheres were collected in the potential range 2.0–0.01 V vs. Li^+/Li (Figure 20) [195]. The structural changes were monitored by following the evolution of the three Raman bands located at 681 cm^{-1} (A_{1g} symmetry involving motion of oxygen in AO_4 tetrahedra), 386 and 324 cm^{-1} (involving the vibration of BO_6 octahedra) according to the usual notations for compounds of generic form AB_2O_4. When the Mn^{3+} ions are reduced to Mn^{2+} during the lithiation process at 1.21 V, the A_{1g} band begins to wane and disappears at 0.16 V, while the strength of Raman bands at 386 and 324 cm^{-1} decreases. At this potential Zn^{2+} and Mn^{2+} are reduced to Zn^0 and Mn^0. During the charge process (delithiation) at 1.25 V, a band grows at 694 cm^{-1} which is characteristic of the asymmetric Mn–O stretch for R-Mn_2O_3 associated with the oxidation of Mn^0 to Mn^{3+}. Above 1.52 V, a band located at 407 cm^{-1} assigned to the E_2 mode of ZnO is the fingerprint of oxidized Zn^0. Therefore, the two weak Raman bands at 324 and 386 cm^{-1} for $ZnMn_2O_4$ reappear at the end of the charge process.

Cabo-Fernandez et al. [196] investigated the delithiation process of carbon-coated $ZnFe_2O_4$ (ZFO) nanoparticles. Like $ZnMn_2O_4$, ZFO is a low-cost anode material with a theoretical specific capacity ~1000 mAh g^{-1} that reacts with lithium via a conversion/alloying process. The first-order Rama spectrum displays 5 bands located at 647 cm^{-1} (A_{1g}), 467 cm^{-1} (T_{2g}), 340 cm^{-1} (T_{2g}), 246 cm^{-1} (E_g) and 221 cm^{-1} (T_{2g}). The conversion reaction that occurs at ~0.8 V leads the formation of Zn^0 particles, which enhance the Raman signal of the SEI components. In the electrode potential between 0.80 and 0.69 V, the Raman spectrum is dominated by the reduction products of electrolyte carbonate solvents which form the SEI.

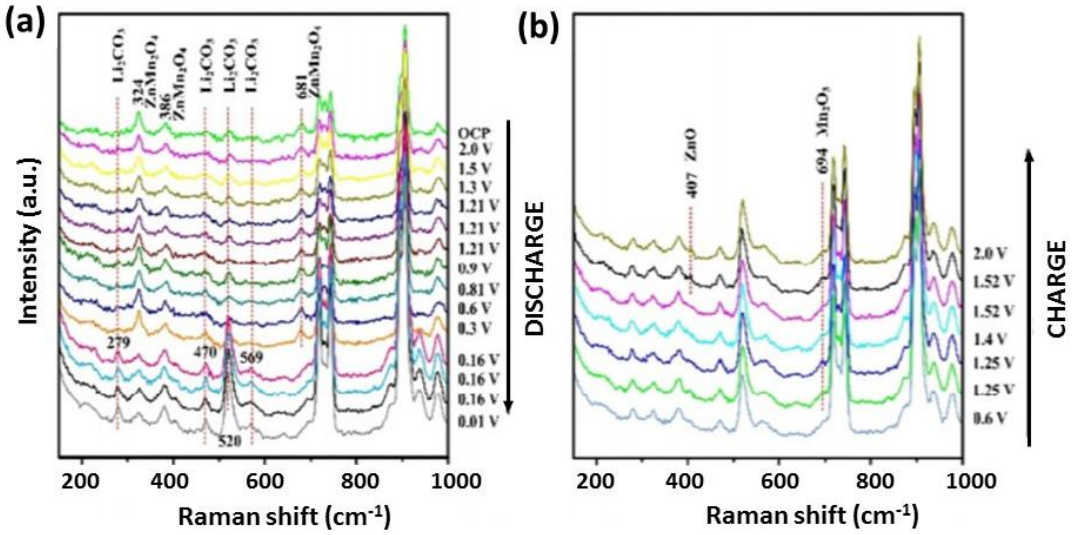

Figure 20. *In situ* Raman spectra showing the lithiation and delithiation of $ZnMn_2O_4$ at representative potentials. Reprinted by permission from Ref. [195].

5. Solid electrolyte interface (SEI)

The solid electrolyte interface is a chemical layer formed on the anode side, i.e., lithium metal or graphite, that is indispensable for the electrochemical stability of Li-ion batteries using organic (aprotic) electrolyte. A SEI is the result of solvation of Li ions, i.e., electrolyte reduction because of the sufficiently low potential of graphite, resulting in the formation of a film deposited on the electrode surface in the first cycle of charge/discharge. After the second cycle, the SEI suppresses the electrolyte decomposition acting as an energetic barrier between the Fermi level of the graphite and the high occupied molecular orbital (HOMO) of the electrolyte. Analysis of the SEI using *in situ* Raman spectroscopy has been reported by few research teams [197–201] only, because the SEI layer is usually very thin so that the Raman signal difficult to be detected. The composition and formation of the SEI were analyzed using copper electrodes after lithium plating. From Raman spectra Schmitz et al. [197] have detected semicarbonates such as Li_2CO_3 and Li_2C_2 as SEI components. *In situ* Raman micro-spectroscopy and Raman mapping reveal that: (i) Li_2C_2 is not formed at a potential >0 V vs. Li^+/Li, (ii) Li_2C_2 is located on the plated lithium and (iii) Li_2CO_3 is homogeneously distributed over the copper sheet. The presence of Li_2C_2 on the metallic Li surface has been considered as a product of laser degradation rather than an actual SEI species [202,203]. The SEI formation onto SiO_2-coated Au nanoparticles was studied using *in situ* surfaced-enhanced Raman spectroscopy (SERS) in lithium-ion battery [201]. The effect of the additive vinylene carbonate (VC) in the ethylene carbonate (EC) electrolyte was investigated by monitoring the band intensity of silicon, which exhibits different amorphization rates between bulk and surface. Park et al. [204] investigated the mechanism of the electrolyte–electrode interface reaction using *in situ* Raman spectroscopy during the second charging process. Due to the low permeability of the SEI, there is a variation of ion concentration during charging and discharging a Li-ion battery [205]. This change in concentration nearby the separator has been investigated by *in situ* Raman spectroscopy using ultrafine microfiber probes [206,207]. Recently, Yamanaka et al. [22,207] performed such measurements with a graphite//$LiFePO_4$ cell using an electrolyte solution of 1 mol L^{-1} $LiClO_4$

dissolved in ethylene carbonate (EC) and diethyl carbonate (DEC) solution. Intensities of three Raman peaks were analyzed: at 718 and 730 cm^{-1} (symmetric ring deformation mode of EC and solvated EC with Li^+ and 935 cm^{-1} (symmetric mode of the anion ClO_4^-). The properties of the SEI were modified by adding film-forming additives to the EC:DEC solution. Based on *in situ* Raman spectro-electrochemistry, the concerted effect of the SEI and the adjacent separator film generates an effective barrier for Li ions [208]. The same research's group [209] performed a chronoamperometric pretreatment of HOPG anode at 0.9 V vs. lithium applied for 20 h that decrease the resistance charge transfer and capacitance at the surface of graphite. The main result of this pretreatment consists in the suppression of the concentration changes.

6. Conclusions

In this review, we have shown that, among the various *in situ* methods, Raman spectro-electrochemistry is a highly effective technique in intensive field of researches covering all aspects of battery operation. Regarding the structural response of electrode materials, the contribution of both in-situ Raman spectro-electrochemistry and Raman mapping were determining for the issue of real time charge–discharge cycling because they are powerful tool for studying the short-range order (local environment) in lattices. *In situ* analyses are carried out to track several effects occurring during charging and discharging process in lithium batteries such as phase stability, structural modifications of the electrode materials during insertion/deinsertion reaction, interface evolution, compatibility between materials, kinetics of Li^+ ions diffusing in the electrodes et electrolytes, electrode degradation and formation of the SEI layer.

As other in operando analytical methods, *in situ* Raman spectroscopy is used not only to improve the cycle stability of entire batteries, but to provide experimental evidence of new insights of Li^+-ion insertion/deinsertion mechanism. However, due to the short optical penetration depth, Raman spectroscopy is essentially a surface analysis technique and the spectral response cannot be extended to the bulk of a sample that makes some difference with results obtained from *in situ* X-ray diffraction when the rate of analysis is not enough slow.

Conflict of interest

The authors declare that there is no conflict of interest regarding the publication of this manuscript.

References

1. Julien CM, Mauger A, Vijh A, et al. (2016) Principles of Intercalation, In: Julien CM, Mauger A, Vijh A, et al., *Lithium Batteries: Science and Technology*, Cham, Switzerland: Springer, 69–91.
2. Novák P, Panitz JC, Joho F, et al. (2000) Advanced in situ methods for the characterization of practical electrodes in lithium-ion batteries. *J Power Sources* 90: 52–58.
3. Shao M (2014) In situ microscopic studies on the structural and chemical behaviors of lithium-ion battery materials. *J Power Sources* 270: 475–486.
4. Harks PPRML, Mulder FM, Notten PHL (2015) In situ methods for Li-ion battery research: A review of recent developments. *J Power Sources* 288: 92–105.

5. Weatherup RS, Bayer BC, Blume R, et al. (2011) In situ characterization of alloy catalysts for low-temperature graphene growth. *Nano Lett* 11: 4154–4160.
6. Yang Y, Liu X, Dai Z, et al. (2017) In situ electrochemistry of rechargeable battery materials: Status report and perspectives. *Adv Mater* 29: 1606922.
7. Shu J, Ma R, Shao L, et al. (2014) In-situ X-ray diffraction study on the structural evolutions of $LiNi_{0.5}Co_{0.3}Mn_{0.2}O_2$ in different working potential windows. *J Power Sources* 245: 7–18.
8. Membreño N, Xiao P, Park KS, et al. (2013) In situ Raman study of phase stability of α-$Li_3V_2(PO_4)_3$ upon thermal and laser heating. *J Phys Chem C* 117: 11994–12002.
9. Kong F, Kostecki R, Nadeau G, et al. (2001) In situ studies of SEI formation. *J Power Sources* 97–98: 58–66.
10. Mehdi BL, Qian J, Nasybulin E, et al. (2015) Observation and quantification of nanoscale processes in lithium batteries by operando electrochemical (S)TEM. *Nano Lett* 15: 2168–2173.
11. Kerlau M, Marcinek M, Srinivasan V, et al. (2007) Studies of local degradation phenomena in composite cathodes for lithium-ion batteries. *Electrochim Acta* 52: 5422–5429.
12. Hausbrand R, Cherkashinin G, Ehrenberg H, et al. (2015) Fundamental degradation mechanisms of layered oxide Li-ion battery cathode materials: Methodology, insights and novel approaches. *Mater Sci Eng B-Adv* 192: 3–25.
13. Julien C (2000) Local environment in 4-volt cathode materials for Li-ion batteries, In: Julien C, Stoynov Z, *Materials for Lithium-ion Batteries*, NATO Science Series (Series 3. High Technology), Dordrecht: Springer, 309–326.
14. Itoh T, Sato H, Nishina T, et al. (1997) In situ Raman spectroscopic study of Li_xCoO_2 electrodes in propylene carbonate solvent systems. *J Power Sources* 68: 333–337.
15. Song SW, Han KS, Fujita H, et al. (2001) In situ visible Raman spectroscopic study of phase change in $LiCoO_2$ film by laser irradiation. *Chem Phys Lett* 344: 299–304.
16. Julien C (2000) Local cationic environment in lithium nickel–cobalt oxides used as cathode materials for lithium batteries. *Solid State Ionics* 136–137: 887–896.
17. Julien CM, Gendron F, Amdouni N, et al. (2006) Lattice vibrations of materials for lithium rechargeable batteries. VI: Ordered spinels. *Mater Sci Eng B-Adv* 130: 41–48.
18. Ramana CV, Smith RJ, Hussain OM, et al. (2004) Growth and surface characterization of V_2O_5 thin films made by pulsed-laser deposition. *J Vac Sci Technol A* 22: 2453–2458.
19. Zhang X, Frech R (1998) In situ Raman spectroscopy of $Li_xV_2O_5$ in a lithium rechargeable battery. *J Electrochem Soc* 145: 847–851.
20. Inaba M, Iriyama Y, Ogumi Z, et al. (1997) Raman study of layered rock-salt $LiCoO_2$ and its electrochemical lithium deintercalation. *J Raman Spectrosc* 28: 613–617.
21. Battisti D, Nazri GA, Klassen B, et al. (1993) Vibrational studies of lithium perchlorate in propylene carbonate solutions. *J Phys Chem* 97: 5826–5830.
22. Yamanaka T, Nakagawa H, Tsubouchi S, et al. (2017) In situ Raman spectroscopic studies on concentration of electrolyte salt in lithium-ion batteries by using ultrafine multifiber probes. *ChemSusChem* 10: 855–861.
23. Yang Y, Liu X, Dai Z, et al. (2017) In situ electrochemistry of rechargeable battery materials: Status report and perspectives. *Adv Mater* 29: 1606922.
24. Lei J, McLarnon F, Kostecki R (2005) In situ Raman microscopy of individual $LiNi_{0.8}Co_{0.15}Al_{0.05}O_2$ particles in a Li-ion battery composite cathode. *J Phys Chem B* 109: 952–957.

25. Nakagawa H, Dom Yi, Doi T, et al. (2014) In situ Raman study of graphite negative-electrodes in electrolyte solution containing fluorinated phosphoric esters. *J Electrochem Soc* 161: A480–A485.
26. Zhang X, Cheng F, Zhang K, et al. (2012) Facile polymer-assisted synthesis of $LiNi_{0.5}Mn_{1.5}O_4$ with a hierarchical micro–nano structure and high rate capability. *RSC Adv* 2: 5669–5675.
27. Amaraj SF, Aurbach D (2011) The use of in situ techniques in R&D of Li and Mg rechargeable batteries. *J Solid State Electr* 15: 877–890.
28. Stancovski V, Badilescu S (2014) In situ Raman spectroscopic–electrochemical studies of lithium-ion battery materials: a historical overview. *J Appl Electrochem* 44: 23–43.
29. Baddour-Hadjean R, Pereira-Ramos JP (2010) Raman microspectrometry applied to the study of electrode materials for lithium batteries. *Chem Rev* 110: 1278–1319.
30. Burba CM, Frech R (2006) Modified coin cells for in situ Raman spectro-electrochemical measurements of $Li_xV_2O_5$ for lithium rechargeable batteries. *Appl Spectrosc* 60: 490–493.
31. Gross T, Giebeler L, Hess C (2013) Novel in situ cell for Raman diagnostics of lithium-ion batteries. *Rev Sci Instrum* 84: 073109.
32. Gross T, Hess C (2014) Raman diagnostics of $LiCoO_2$ electrodes for lithium-ion batteries. *J Power Sources* 256: 220–225.
33. Sole C, Drewett NE, Hardwick LJ (2014) In situ Raman study of lithium-ion intercalation into microcrystalline graphite. *Faraday Discuss* 172: 223–237.
34. Novák P, Goers D, Hardwick L, et al. (2005) Advanced in situ characterization methods applied to carbonaceous materials. *J Power Sources* 146: 15–20.
35. Fang S, Yan M, Hamers RJ (2017) Cell design and image analysis for in situ Raman mapping of inhomogeneous state-of-charge profiles in lithium-ion batteries. *J Power Sources* 352: 18–25.
36. Ghanty C, Markovsky B, Erickson EM, et al. (2015) Li^+-ion extraction/insertion of Ni-rich $Li_{1+x}(Ni_yCo_zMn_z)_wO_2$ ($0.005 < x < 0.03$; y:z = 8:1, $w \approx 1$) electrodes: in situ XRD and Raman spectroscopy study. *ChemElectroChem* 2: 1479–1486.
37. Huang JX, Li B, Liu B, et al. (2016) Structural evolution of NM (Ni and Mn) lithium-rich layered material revealed by in-situ electrochemical Raman spectroscopic study. *J Power Sources* 310: 85–90.
38. Dash WC, Newman R (1955) Intrinsic optical absorption in single-crystal germanium and silicon at 77 K and 300 K. *Phys Rev* 99: 1151–1155.
39. Brodsky MH, Title RS, Weiser K, et al. (1970) Structural, optical, and electrical properties of amorphous silicon films. *Phys Rev B* 1: 2632–2641.
40. Pollak E, Salitra G, Baranchugov V, et al. (2007) In situ conductivity, impedance spectroscopy, and ex situ Raman spectra of amorphous silicon during the insertion/extraction of lithium. *J Phys Chem C* 111: 11437–11444.
41. Tuinstra F, Koenig JL (1970) Raman spectrum of graphite. *J Chem Phys* 53: 1126–1130.
42. Kostecki R, Schnyder B, Alliata D, et al. (2001) Surface studies of carbon films from pyrolyzed photoresist. *Thin Solid Films* 396: 36–43.
43. Julien CM, Zaghib K, Mauger A, et al. (2006) Characterization of the carbon coating onto $LiFePO_4$ particles used in lithium batteries. *J Appl Phys* 100: 063511.
44. Panitz JC, Joho F, Novák P (1999) In situ characterization of a graphite electrode in a secondary lithium-ion battery using Raman microscopy. *Appl Spectrosc* 53: 1188–1199.

45. Panitz JC, Novák P, Haas O (2001) Raman microscopy applied to rechargeable lithium-ion cells —Steps towards in situ Raman imaging with increased optical efficiency. *Appl Spectrosc* 55: 1131–1137.
46. Panitz JC, Novák P (2001) Raman spectroscopy as a quality control tool for electrodes of lithium-ion batteries. *J Power Sources* 97–98: 174–180.
47. Kostecki R, Lei J, McLarnon F, et al. (2006) Diagnostic evaluation of detrimental phenomena in high-power lithium-ion batteries. *J Electrochem Soc* 153: A669–A672.
48. Forster JD, Harris SJ, Urban JJ (2014) Mapping Li^+ concentration and transport via in situ confocal Raman microscopy. *J Phys Chem Lett* 5: 2007–2011.
49. Nishi T, Nakai H, Kita A (2013) Visualization of the state-of-charge distribution in a $LiCoO_2$ cathode by in situ Raman imaging. *J Electrochem Soc* 160: A1785–A1788.
50. Nanda J, Remillard J, O'Neill A, et al. (2011) Local state-of-charge mapping of lithium-ion battery electrodes. *Adv Funct Mater* 21: 3282–3290.
51. Slautin B, Alikin D, Rosato D, et al. (2018) Local study of lithiation and degradation paths in $LiMn_2O_4$ battery cathodes: confocal Raman microscopy approach. *Batteries* 4: 21.
52. Li J, Shunmugasundaram R, Doig R, et al. (2016) In situ X-ray diffraction study of layered Li–Ni–Mn–Co oxides: Effect of particle size and structural stability of core–shell materials. *Chem Mater* 28: 162–171.
53. Graetz J, Gabrisch H, Julien CM, et al. (2003) Raman evidence of spinel formation in delithiated cobalt oxide. *Electrochemical society Proceedings Volume 2003-28; Proceedings-electrochemical Society PV, Symposium, Lithium and lithium-ion battery*, 28: 95–100.
54. Yu L, Liu H, Wang Y, et al. (2013) Preferential adsorption of solvents on the cathode surface of lithium ion batteries. *Angew Chem Int Edit* 52: 5753–5756.
55. Kuwata N, Ise K, Matsuda Y, et al. (2012) Detection of degradation in $LiCoO_2$ thin films by in situ micro Raman spectroscopy, In: Chowdari BVR, Kawamura J, Mizusaki J, et al. (Eds.), *Solid State Ionics: Ionics for Sustainable World, Proceedings of the 13th Asian Conference*, Singapore: World Scientific, 138–143.
56. Gross T, Hess C (2014) Spatially-resolved in situ Raman analysis of $LiCoO_2$ electrodes. *ECS Trans* 61: 1–9.
57. Fukumitsu H, Omori M, Terada K, et al. (2015) Development of in situ cross-sectional Raman imaging of $LiCoO_2$ cathode for Li-ion battery. *Electrochemistry* 83: 993–996.
58. Heber M, Schilling C, Gross T, et al. (2015) In situ Raman and UV-Vis spectroscopic analysis of lithium-ion batteries. *MRS Proceedings* 1773: 33–40.
59. Otoyama M, Ito Y, Hayashi A, et al. (2016) Raman imaging for $LiCoO_2$ composite positive electrodes in all-solid-state lithium batteries using Li_2S–P_2S_5 solid electrolytes. *J Power Sources* 302: 419–425.
60. Porthault H, Baddour-Hadjean R, Le Cras F, et al. (2012) Raman study of the spinel-to-layered phase transformation in sol–gel $LiCoO_2$ cathode powders as a function of the post-annealing temperature. *Vib Spectrosc* 62: 152–158.
61. Park Y, Kim NH, Kim JY, et al. (2010) Surface characterization of the high voltage $LiCoO_2$/Li cell by X-ray photoelectron spectroscopy and 2D correlation analysis. *Vib Spectrosc* 53: 60–63.
62. Zhang X, Mauger A, Lu Q, et al. (2010) Synthesis and characterization of $LiNi_{1/3}Mn_{1/3}Co_{1/3}O_2$ by wet-chemical method. *Electrochim Acta* 55: 6440–6449.

63. Ben-Kamel K, Amdouni N, Mauger A, et al. (2012) Study of the local structure of $LiNi_{0.33+\delta}Mn_{0.33+\delta}Co_{0.33-2\delta}O_2$ ($0.025 \leq \delta \leq 0.075$) oxides. *J Alloy Compd* 528: 91–98.
64. Hayden C, Talin AA (2014) Raman spectroscopic analysis of $LiNi_{0.5}Co_{0.2}Mn_{0.3}O_2$ cathodes stressed to high voltage.
65. Otoyama M, Ito Y, Hayashi A, et al. (2016) Raman spectroscopy for $LiNi_{1/3}Mn_{1/3}Co_{1/3}O_2$ composite positive electrodes in all-solid-state lithium batteries. *Electrochemistry* 84: 812–816.
66. Lanz P, Villevieille C, Novák P (2014) Ex situ and in situ Raman microscopic investigation of the differences between stoichiometric $LiMO_2$ and high-energy $xLi_2MnO_3 (1 - x)LiMO_2$ (M = Ni, Co, Mn). *Electrochim Acta* 130: 206–212.
67. Koga H, Croguennec L, Mannessiez P, et al. (2012) $Li_{1.20}Mn_{0.54}Co_{0.13}Ni_{0.13}O_2$ with different particle sizes as attractive positive electrode materials for lithium-ion batteries: Insights into their structure. *J Phys Chem C* 116: 13497–13506.
68. Julien CM, Massot M (2003) Lattice vibrations of materials for lithium rechargeable batteries III. Lithium manganese oxides. *Mater Sci Eng B-Adv* 100: 69–78.
69. Singh G, West WC, Soler J, et al. (2012) In situ Raman spectroscopy of layered solid solution Li_2MnO_3–$LiMO_2$ (M = Ni, Mn, Co). *J Power Sources* 218: 34–38.
70. Lanz P, Villevieille C, Novák P (2013) Electrochemical activation of Li_2MnO_3 at elevated temperature investigated by in situ Raman microscopy. *Electrochim Acta* 109: 426–432.
71. Rao CV, Soler J, Katiyar R, et al. (2014) Investigations on electrochemical behavior and structural stability of $Li_{1.2}Mn_{0.54}Ni_{0.13}Co_{0.13}O_2$ lithium-ion cathodes via in-situ and ex-situ Raman spectroscopy. *J Phys Chem C* 118: 14133–14141.
72. Hy S, Felix F, Rick J, et al. (2014) Direct in situ observation of Li_2O evolution on Li-rich high-capacity cathode material, $Li[Ni_xLi_{(1-2x)/3}Mn_{(2-x)/3}]O_2$ ($0 \leq x \leq 0.5$). *J Am Chem Soc* 136: 999–1007.
73. Shojan J, Rao-Chitturi V, Soler J, et al. (2015) High energy $xLi_2MnO_3 (1 - x)LiNi_{2/3}Co_{1/6}Mn_{1/6}O_2$ composite cathode for advanced Li-ion batteries. *J Power Sources* 274: 440–450.
74. Grey CP, Yoon W, Reed J, et al. (2004) Electrochemical activity of Li in the transition-metal sites of O3 $Li[Li_{(1-2x)/3}Mn_{(2-x)/3}Ni_x]O_2$. *Electrochem Solid St* 7: A290–A 293.
75. Amalraj F, Talianker M, Markovsky B, et al. (2013) Study of the lithium-rich integrated compound $xLi_2MnO_3 (1 - x)LiMO_2$ (x around 0.5; M = Mn, Ni, Co; 2:2:1) and its electrochemical activity as positive electrode in lithium cells. *J Electrochem Soc* 160: A324–A337.
76. Kumar-Nayak P, Grinblat J, Levi M, et al. (2014) Electrochemical and structural characterization of carbon coated $Li_{1.2}Mn_{0.56}Ni_{0.16}Co_{0.08}O_2$ and $Li_{1.2}Mn_{0.6}Ni_{0.2}O_2$ as cathode materials for Li-ion batteries. *Electrochim Acta* 137: 546–556.
77. Wu Q, Maroni VA, Gosztola DJ, et al. (2015) A Raman-based investigation of the fate of Li_2MnO_3 in lithium- and manganese-rich cathode materials for lithium ion batteries. *J Electrochem Soc* 162: A1255–A1264.
78. Bak SM, Nam KW, Chang W, et al. (2013) Correlating structure changes and gas evolution during the thermal decomposition of charged $Li_xNi_{0.8}Co_{0.15}Al_{0.05}O_2$ cathode material. *Chem Mater* 25: 337–351.
79. Julien C, Camacho-Lopez MA, Lemal M, et al. (2002) $LiCo_{1-y}M_yO_2$ positive electrodes for rechargeable lithium batteries. I. Aluminum doped materials. *Mater Sci Eng B-Adv* 95: 6–13.

80. Julien CM, Mauger A, Vijh A, et al. (2016) Cathode Materials with Monoatomic Ions in a Three-Dimensional Framework, In: Julien CM, Mauger A, Vijh A, et al., *Lithium Batteries: Science and Technology*, Cham, Switzerland: Springer, 163–199.
81. Ohzuku T, Kitagawa M, Hirai T (1990) Electrochemistry of manganese dioxide in lithium nonaqueous cell. III. X-ray diffractional study on the reduction of spinel-related manganese dioxide. *J Electrochem Soc* 137: 769–775.
82. Liu W, Kowal K, Farrington GC (1998) Mechanism of the electrochemical insertion of lithium into $LiMn_2O_4$ spinels. *J Electrochem Soc* 145: 459–465.
83. Xia Y, Yoshio M (1996) An investigation of lithium ion insertion into spinel structure Li–Mn–O compounds. *J Electrochem Soc* 143: 825–833.
84. Richard MN, Keotschau I, Dahn JR (1997) A cell for in situ x-ray diffraction based on coin cell hardware and Bellcore plastic electrode technology. *J Electrochem Soc* 144: 554–557.
85. Yang XQ, Sun X, Lee SJ, et al. (1999) In situ synchrotron X-ray diffraction studies of the phase transitions in $Li_xMn_2O_4$ cathode Materials. *Electrochem Solid St* 2: 157–160.
86. Kanamura K, Naito H, Yao T, et al. (1996) Structural change of the $LiMn_2O_4$ spinel structure induced by extraction of lithium. *J Mater Chem* 6: 33–36.
87. White WB, DeAngelis A (1967) Interpretation of the vibrational spectra of spinels. *Spectrochim Acta A* 23: 985–995.
88. Ammundsen B, Burns GR, Islam MS, et al. (1999) Lattice dynamics and vibrational spectra of lithium manganese oxides: A computer simulation and spectroscopic study. *J Phys Chem B* 103: 5175–5180.
89. Kanoh H, Tang W, Ooi K (1998) In situ Raman spectroscopic study on electroinsertion of Li^+ into a Pt/λ-MnO_2 electrode in aqueous solution. *Electrochem Solid St* 1: 17–19.
90. Huang W, Frech R (1999) In situ Raman spectroscopic studies of electrochemical intercalation in $Li_xMn_2O_4$-based cathodes. *J Power Sources* 81–82: 616–620.
91. Julien C, Massot M (2003) Lattice vibrations of materials for lithium rechargeable batteries I. Lithium manganese oxide spinel. *Mater Sci Eng B-Adv* 97: 217–230.
92. Dokko K, Shi Q, Stefan IC, et al. (2003) In situ Raman spectroscopy of single microparticle Li^+-intercalation electrodes. *J Phys Chem B* 107: 12549–12554.
93. Anzue N, Itoh T, Mohamedi M, et al. (2003) In situ Raman spectroscopic study of thin-film $Li_{1-x}Mn_2O_4$ electrodes. *Solid State Ionics* 156: 301–307.
94. Shi Q, Takahashi Y, Akimoto J, et al. (2005) In situ Raman scattering measurements of a $LiMn_2O_4$ single crystal microelectrode. *Electrochem Solid St* 8: A521–A524.
95. Sun X, Yang XQ, Balasubramanian M, et al. (2002) In situ investigation of phase transitions of $Li_{1+y}Mn_2O_4$ spinel during Li-ion extraction and insertion. *J Electrochem Soc* 149: A842–A848.
96. Michalska M, Ziołkowska DA, Jasinski JB, et al. (2018) Improved electrochemical performance of $LiMn_2O_4$ cathode material by Ce doping. *Electrochim Acta* 276: 37–46.
97. Liu J, Manthiram A (2009) Understanding the improved electrochemical performances of Fe-substituted 5 V spinel cathode $LiMn_{1.5}Ni_{0.5}O_4$. *J Phys Chem C* 113: 15073–15079.
98. Alcantara R, Jaraba M, Lavela P, et al. (2003) Structural and electrochemical study of new $LiNi_{0.5}Ti_xMn_{1.5-x}O_4$ spinel oxides for 5-V cathode materials. *Chem Mater* 15: 2376–2382.
99. Zhong GB, Wang YY, Yu YQ, et al. (2012) Electrochemical investigations of the $LiNi_{0.45}M_{0.10}Mn_{1.45}O_4$ (M = Fe, Co, Cr) 5 V cathode materials for lithium ion batteries. *J Power Sources* 205: 385–393.

100. Liu D, Hamel-Paquet J, Trottier J, et al. (2012) Synthesis of pure phase disordered $LiMn_{1.45}Cr_{0.1}Ni_{0.45}O_4$ by a post-annealing method. *J Power Sources* 217: 400–406.
101. Zhu W, Liu D, Trottier J, et al. (2014) Comparative studies of the phase evolution in M-doped $Li_xMn_{1.5}Ni_{0.5}O_4$ (M = Co, Al, Cu and Mg) by in-situ X-ray diffraction. *J Power Sources* 264: 290–298.
102. Dokko K, Mohamedi M, Anzue N, et al. (2002) In situ Raman spectroscopic studies of $LiNi_xMn_{2-x}O_4$ thin film cathode materials for lithium ion secondary batteries. *J Mater Chem* 12: 3688–3693.
103. Zhu W, Liu D, Trottier J, et al. (2014) In situ Raman spectroscopic investigation of $LiMn_{1.45}Ni_{0.45}M_{0.1}O_4$ (M = Cr, Co) 5 V cathode materials. *J Power Sources* 298: 341–348.
104. Cocciantelli JM, Doumerc JP, Pouchard M, et al. (1991) Crystal chemistry of electrochemically inserted $Li_xV_2O_5$. *J Power Sources* 34: 103–111.
105. Zhang X, Frech R (1996) In situ Raman spectroscopy of $Li_xV_2O_5$ in a lithium rechargeable battery. *ECS Proceedings* 17: 198–203.
106. Baddour-Hadjean R, Navone C, Pereira-Ramos JP (2009) *In situ* Raman microspectrometry investigation of electrochemical lithium intercalation into sputtered crystalline V_2O_5 thin films. *Electrochim Acta* 54: 6674–6679.
107. Jung H, Gerasopoulos K, Talin AA, et al. (2017) In situ characterization of charge rate dependent stress and structure changes in V_2O_5 cathode prepared by atomic layer deposition. *J Power Sources* 340: 89–97.
108. Jung H, Gerasopoulos K, Talin AA, et al. (2017) A platform for in situ Raman and stress characterizations of V_2O_5 cathode using MEMS device. *Electrochim Acta* 242: 227–239.
109. Julien C, Ivanov I, Gorenstein A (1995) Vibrational modifications on lithium intercalation in V_2O_5 films. *Mater Sci Eng B-Adv* 33: 168–172.
110. Baddour-Hadjean R, Pereira-Ramos JP, Navone C, et al. (2008) Raman microspectrometry study of electrochemical lithium intercalation into sputtered crystalline V_2O_5 thin films. *Chem Mater* 20: 1916–1923.
111. Baddour-Hadjean R, Raekelboom E, Pereira-Ramos JP (2006) New structural characterization of the $Li_xV_2O_5$ system provided by Raman spectroscopy. *Chem Mater* 18: 3548–3556.
112. Baddour-Hadjean R, Marzouk A, Pereira-Ramos JP (2012) Structural modifications of $Li_xV_2O_5$ in a composite cathode ($0 < x < 2$) investigated by Raman microspectrometry. *J Raman Spectrosc* 43: 153–160.
113. Baddour-Hadjean R, Pereira-Ramos JP (2007) New structural approach of lithium intercalation using Raman spectroscopy. *J Power Sources* 174: 1188–1192.
114. Julien C, Massot M (2002) Spectroscopic studies of the local structure in positive electrodes for lithium batteries. *Phys Chem Chem Phys* 4: 4226–4235.
115. Chen D, Ding D, Li X, et al. (2015) Probing the charge storage mechanism of a pseudocapacitive MnO_2 electrode using in operando Raman spectroscopy. *Chem Mater* 27: 6608–6619.
116. Julien CM, Massot M, Poinsignon C (2004) Lattice vibrations of manganese oxides: Part I. Periodic structures. *Spectrochim Acta A* 60: 689–700.
117. Hashem AM, Abuzeid H, Kaus M, et al. (2018) Green synthesis of nanosized manganese dioxide as positive electrode for lithium-ion batteries using lemon juice and citrus peel. *Electrochim Acta* 262: 74–81.

118. Julien C, Massot M, Baddour-Hadjean R, et al. (2003) Raman spectra of birnessite manganese dioxides. *Solid State Ionics* 159: 345–356.
119. Hwang SJ, Park HS, Choy JH, et al. (2001) Micro-Raman spectroscopic study on layered lithium manganese oxide and its delithiated/relithiated derivatives. *Electrochem Solid St* 4: A213–A216.
120. Chen D, Ding D, Li X, et al. (2015) Probing the charge storage mechanism of a pseudocapacitive MnO_2 electrode using in operando Raman spectroscopy. *Chem Mater* 27: 6608–6619.
121. Yang L, Cheng S, Wang J, et al. (2016) Investigation into the origin of high stability of δ-MnO_2 pseudo-capacitive electrode using operando Raman spectroscopy. *Nano Energy* 30: 293–302.
122. Zaghib K, Dontigny M, Perret P, et al. (2014) Electrochemical and thermal characterization of lithium titanate spinel anode in C-$LiFePO_4$//C-$Li_4Ti_5O_{12}$ cells at sub-zero temperatures. *J Power Sources* 248: 1050–1057.
123. Paques-Ledent MT, Tarte P (1974) Vibrational studies of olivine-type compounds 2. Orthophosphates, orthoarsenates and orthovanadates $A^IB^{II}X^VO^4$. *Spectrochim Acta A* 30: 673–689.
124. Wu J, Dathar GK, Sun C, et al. (2013) In situ Raman spectroscopy of $LiFePO_4$: size and morphology dependence during charge and self-discharge. *Nanotechnology* 24: 424009.
125. Ramana CV, Mauger A, Gendron F, et al. (2009) Study of the Li-insertion/extraction process in $LiFePO_4$/$FePO_4$. *J Power Sources* 187: 555–564.
126. Siddique NA, Salehi A, Wei Z, et al. (2015) Length-scale-dependent phase transformation of $LiFePO_4$: An in situ and operando study using micro-Raman spectroscopy and XRD. *ChemPhysChem* 16: 2383–2388.
127. Burba CM, Frech R (2004) Raman and FTIR spectroscopic study of Li*x*$FePO_4$ ($0 \le x \le 1$). *J Electrochem Soc* 151: A1032–A1038.
128. Morita M, Asai Y, Yoshimoto N, et al. (1998) A Raman spectroscopic study of organic electrolyte solutions based on binary solvent systems of ethylene carbonate with low viscosity solvents which dissolve different lithium salts. *J Chem Soc Faraday Trans* 94: 3451–3456.
129. Burba CM, Frech R (2007) Vibrational spectroscopic studies of monoclinic and rhombohedral $Li_3V_2(PO_4)_3$. *Solid State Ionics* 177: 3445–3454.
130. Yin SC, Grondey H, Strobel P, et al. (2003) Electrochemical property: Structure relationships in monoclinic $Li_3V_2(PO_4)_3$. *J Am Chem Soc* 125: 10402–10411.
131. Takeuchi KJ, Marschilok AC, Davis SM, et al. (2001) Silver vanadium oxide and related battery applications. *Coordin Chem Rev* 219–221: 283–310.
132. Bao Q, Bao S, Li CM, et al. (2007) Lithium insertion in channel-structured β-$AgVO_3$: in situ Raman study and computer simulation. *Chem Mater* 19: 5965–5972.
133. Tuinstra F, Koenig JL (1970) Raman spectrum of graphite. *J Chem Phys* 53: 1126–1130.
134. Reich S, Thomsen C (2004) Raman spectroscopy of graphite. *Philos T R Soc A* 362: 2271–2288.
135. Inaba M, Yoshida H, Yida H, et al. (1995) In situ Raman study on electrochemical Li intercalation into graphite. *J Electrochem Soc* 142: 20–26.
136. Huang W, Frech R (1998) In situ Raman studies of graphite surface structures during lithium electrochemical intercalation. *J Electrochem Soc* 145: 765–770.
137. Nov åk P, Joho F, Imhof R, et al. (1999) In situ investigation of the interaction between graphite and electrolyte solutions. *J Power Sources* 81–82: 212–216.

138. Luo Y, Cai WB, Scherson DA (2002) In situ, real-time Raman microscopy of embedded single particle graphite electrodes. *J Electrochem Soc* 149: A1100–A1105.
139. Kostecki R, McLarnon F (2003) Microprobe study of the effect of Li intercalation on the structure of graphite. *J Power Sources* 119–121: 550–554.
140. Luo Y, Cai WB, Xing XK, et al. (2004) In situ, time-resolved Raman spectromicrotopography of an operating lithium-ion battery. *Electrochem Solid St* 7: E1–E5.
141. Shi Q, Dokko K, Scherson DA (2004) In situ Raman microscopy of a single graphite microflake electrode in a Li^+-containing electrolyte. *J Phys Chem B* 108: 4798–4793.
142. Migge S, Sandmann G, Rahner D, et al. (2005) Studying lithium intercalation into graphite particles via in situ Raman spectroscopy and confocal microscopy. *J Solid State Electr* 9: 132–137.
143. Hardwick LJ, Hahn M, Ruch P, et al. (2006) Graphite surface disorder detection using in situ Raman microscopy. *Solid State Ionics* 177: 2801–2806.
144. Hardwick LJ, Buqa H, Holzapfel M, et al. (2007) Behaviour of highly crystalline graphitic materials in lithium-ion cells with propylene carbonate containing electrolytes: An in situ Raman and SEM study. *Electrochim Acta* 52: 4884–4891.
145. Hardwick LJ, Marcinek M, Beer L, et al. (2008) An investigation of the effect of graphite degradation on irreversible capacity in lithium-ion cells. *J Electrochem Soc* 155: A442–A447.
146. Hardwick LJ, Ruch PW, Hahn M, et al. (2008) In situ Raman spectroscopy of insertion electrodes for lithium-ion batteries and supercapacitors: First cycle effects. *J Phys Chem Solids* 69: 1232–1237.
147. Nakagawa H, Ochida M, Domi Y, et al. (2012) Electrochemical Raman study of edge plane graphite negative-electrodes in electrolytes containing trialkyl phosphoric ester. *J Power Sources* 212: 148–153.
148. Underhill C, Leung SY, Dresselhaus G, et al. (1979) Infrared and Raman spectroscopy of graphite-ferric chloride. *Solid State Commun* 29: 769–774.
149. Hardwick LJ, Hahn M, Ruch P, et al. (2006) An in situ Raman study of the intercalation of supercapacitor-type electrolyte into microcrystalline graphite. *Electrochim Acta* 52: 675–680.
150. Solin SA (1990) *Graphite Intercalation Compounds*, Berlin: Springer-Verlag.
151. Brancolini G, Negri F (2004) Quantum chemical modeling of infrared and Raman activities in lithium-doped amorphous carbon nanostructures: hexa-*peri*-hexabenzocoronene as a model for hydrogen-rich carbon materials. *Carbon* 42: 1001–1005.
152. Nakagawa H, Domi Y, Doi T, et al. (2012) In situ Raman study on degradation of edge plane graphite negative-electrodes and effects of film-forming additives. *J Power Sources* 206: 320–324.
153. Perez-Villar S, Lanz P, Schneider H, et al. (2013) Characterization of a model solid electrolyte interphase/carbon interface by combined in situ Raman/Fourier transform infrared microscopy. *Electrochim Acta* 106: 506–515.
154. Nakagawa H, Domi Y, Doi T, et al. (2013) In situ Raman study on the structural degradation of a graphite composite negative-electrode and the influence of the salt in the electrolyte solution. *J Power Sources* 236: 138–144.
155. Lanz P, Novák P (2014) Combined in situ Raman and IR microscopy at the interface of a single graphite particle with ethylene carbonate/dimethyl carbonate. *J Electrochem Soc* 161: A1555–A1563.

156. Domi Y, Doi T, Nakagawa H, et al. (2016) In situ Raman study on reversible structural changes of graphite negative-electrodes at high potentials in $LiPF_6$-Based electrolyte solution. *J Electrochem Soc* 163: A2435–A2440.
157. Yamanaka T, Nakagawa H, Tsubouchi S, et al. (2017) Correlations of concentration changes of electrolyte salt with resistance and capacitance at the surface of a graphite electrode in a lithium ion battery studied by in situ microprobe Raman spectroscopy. *Electrochim Acta* 251: 301–306.
158. Bhattacharya S, Alpas AT (2018) A novel elevated temperature pre-treatment for electrochemical capacity enhancement of graphene nanoflake-based anodes. *Mater Renew Sustain Energy* 7: 3.
159. Inaba M, Yoshida H, Ogumi Z (1996) *In situ* Raman study of electrochemical lithium insertion into mesocarbon microbeads heat-treated at various temperatures. *J Electrochem Soc* 143: 2572–2578.
160. Totir DA, Scherson DA (2000) Electrochemical and in situ Raman studies of embedded carbon particle electrodes in nonaqueous liquid electrolytes. *Electrochem Solid St* 3: 263–265.
161. Ramesha GK, Sampath S (2009) Electrochemical reduction of oriented graphene oxide films: an in situ Raman spectroelectrochemical study. *J Phys Chem C* 113: 7985–7989.
162. Tang W, Goh BM, Hu MY, et al. (2016) In situ Raman and nuclear magnetic resonance study of trapped lithium in the solid electrolyte interface of reduced graphene oxide. *J Phys Chem C* 120: 2600–2608.
163. Julien CM, Massot M, Zaghib K (2007) Structural studies of $Li_{4/3}Me_{5/3}O_4$ (Me = Ti, Mn) electrode materials: local structure and electrochemical aspects. *J Power Sources* 136: 72–79.
164. Mukai K, Kato Y, Nakano H (2014) Understanding the zero-strain lithium insertion scheme of $Li[Li_{1/3}Ti_{5/3}]O_4$: structural changes at atomic scale clarified by Raman spectroscopy. *J Phys Chem C* 118: 2992–2999.
165. Shu J, Shui M, Xu D, et al. (2011) Design and comparison of ex situ and in situ devices for Raman characterization of lithium titanate anode material. *Ionics* 17: 503–509.
166. Julien CM, Mauger A, Vijh A, et al. (2016) Anodes for Li-Ion Batteries, In: Julien CM, Mauger A, Vijh A, et al., *Lithium Batteries: Science and Technology*, Cham, Switzerland: Springer, 323–429.
167. Ohzuku T, Takehara Z, Yoshizawa S (1979) Non-aqueous lithium/titanium dioxide cell. *Electrochim Acta* 24: 219–222.
168. Wagemaker M, Borghols WJH, Mulder FM (2007) Large impact of particle size on insertion reactions. A case for anatase Li_xTiO_2. *J Am Chem Soc* 129: 4323–4327.
169. Mukai K, Kato Y, Nakano H (2014) Understanding the zero-strain lithium insertion scheme of $Li[Li_{1/3}Ti_{5/3}]O_4$: structural changes at atomic scale clarified by Raman spectroscopy. *J Phys Chem C* 118: 2992–2999.
170. Dinh NN, Oanh NTT, Long PD, et al. (2003) Electrochromic properties of TiO_2 anatase thin films prepared by a dipping sol–gel method. *Thin Solid Films* 423: 70–76.
171. Smirnov M, Baddour-Hadjean R (2004) Li intercalation in TiO_2 anatase: Raman spectroscopy and lattice dynamic studies. *J Chem Phys* 121: 2348–2355.
172. Baddour-Hadjean R, Bach S, Smirnov M, et al. (2004) Raman investigation of the structural changes in anatase Li_xTiO_2 upon electrochemical lithium insertion. *J Raman Spectrosc* 35: 577–585.

173. Hardwick LJ, Holzapfel M, Novâk P, et al. (2007) Electrochemical lithium insertion into anatase-type TiO_2: An in situ Raman microscopy investigation. *Electrochim Acta* 52: 5357–5367.
174. Ren Y, Hardwick LJ, Bruce PG (2010) Lithium intercalation into mesoporous anatase with an ordered 3D pore structure. *Angew Chem Int Edit* 49: 2570–2574.
175. Gentili V, Brutti S, Hardwick LJ, et al. (2012) Lithium insertion into anatase nanotubes. *Chem Mater* 24: 4468–4476.
176. Laskova BP, Frank O, Zukalova M, et al. (2013) Lithium insertion into titanium dioxide (anatase): A Raman study with $^{16/18}O$ and $^{6/7}Li$ isotope labeling. *Chem Mater* 25: 3710–3717.
177. Laskova BP, Kavan L, Zukalova M, et al. (2016) In situ Raman spectroelectrochemistry as a useful tool for detection of TiO_2(anatase) impurities in TiO_2(B) and TiO_2(rutile). *Monatsh Chem* 147: 951–959.
178. Mauger A, Xie H, Julien CM, (2016) Composite anodes for lithium-ion batteries, status and trends. *AIMS Mater Sci* 3: 1054–1106.
179. Li H, Huang X, Chen L, et al. (2000) The crystal structural evolution of nano-Si anode caused by lithium insertion and extraction at room temperature. *Solid State Ionics* 135: 181–191.
180. Nanda J, Datta MK, Remillard JT, et al. (2009) In situ Raman microscopy during discharge of a high capacity silicon–carbon composite Li-ion battery negative electrode. *Electrochem Commun* 11: 235–237.
181. Zeng Z, Liu N, Zeng Q, et al. (2016) In situ measurement of lithiation-induced stress in silicon nanoparticles using micro-Raman spectroscopy. *Nano Energy* 22: 105–110.
182. Tardif S, Pavlenko E, Quazuguel L, et al. (2017) Operando Raman spectroscopy and synchrotron X-ray diffraction of lithiation/delithiation in silicon nanoparticle anodes. *ACS Nano* 11: 11306–11316.
183. Miroshnikov Y, Zitoun D (2017) Operando plasmon-enhanced Raman spectroscopy in silicon anodes for Li-ion battery. *J Nanopart Res* 19: 372.
184. Holzapfel M, Buqa H, Hardwick LJ, et al. (2006) Nano silicon for lithium-ion batteries. *Electrochim Acta* 52: 973–978.
185. Long BR, Chan MKY, Greeley JP, et al. (2011) Dopant modulated Li insertion in Si for battery anodes: theory and experiment. *J Phys Chem C* 115: 18916–18921.
186. Miroshnikov Y, Yang J, Shokhen V, et al. (2018) Operando micro-Raman study revealing enhanced connectivity of plasmonic metals decorated silicon anodes for lithium-ion batteries. *ACS Appl Energy Mater* 1: 1096–1105.
187. Zeng Z, Liu N, Zeng Q, et al. (2016) In situ measurement of lithiation-induced stress in silicon nanoparticles using micro-Raman spectroscopy. *Nano Energy* 22: 105–110.
188. Yang J, Kraytsberg A, Ein-Eli Y (2015) In situ Raman spectroscopy mapping of Si based anode material lithiation. *J Power Sources* 282: 294–298.
189. Shimizu M, Usui H, Suzumura T, et al. (2015) Analysis of the deterioration mechanism of Si electrode as a Li-ion battery anode using Raman microspectroscopy. *J Phys Chem C* 119: 2975–2982.
190. Domi Y, Usui H, Shimizu M, et al. (2016) Effect of phosphorus-doping on electrochemical performance of silicon negative electrodes in lithium-ion batteries. *ACS Appl Mater Inter* 8: 7125–7132.

191. Yamaguchi K, Domi Y, Usui H, et al. (2017) Elucidation of the reaction behavior of silicon negative electrodes in a bis(fluorosulfonyl)amide based ionic liquid electrolyte. *ChemElectroChem* 4: 3257–3263.
192. Zhang WJ (2011) A review of the electrochemical performance of alloy anodes for lithium-ion batteries. *J Power Sources* 196: 13–24.
193. Weppner W, Huggins RA (1977) Determination of the kinetic parameters of mixed-conducting electrodes and application to the system Li_3Sb. *J Electrochem Soc* 124: 1569–1578.
194. Drewett NE, Aldous AL, Zou J, et al. (2017) *In situ* Raman spectroscopic analysis of the lithiation and sodiation of antimony microparticles. *Electrochim Acta* 247: 296–305.
195. Zhong X, Wang X, Wang H, et al. (2018) Ultrahigh-performance mesoporous $ZnMn_2O_4$ microspheres as anode materials for lithium-ion batteries and their in situ Raman investigation. *Nano Res* 11: 3814.
196. Cabo-Fernandez L, Mueller F, Passerini S, et al. (2016) In situ Raman spectroscopy of carbon-coated $ZnFe_2O_4$ anode material in Li-ion batteries—Investigation of SEI growth. *Chem Commun* 52: 3970–3973.
197. Schmitz R, Muller RA, Schmitz RW, et al. (2013) SEI investigations on copper electrodes after lithium plating with Raman spectroscopy and mass spectrometry. *J Power Sources* 233: 110–114.
198. Hy S, Felix F, Chen YH, et al. (2014) In situ surface enhanced Raman spectroscopic studies of solid electrolyte interphase formation in lithium ion battery electrodes. *J Power Sources* 256: 324–328.
199. Yamanaka T, Nakagawa H, Tsubouchi S, et al. (2017) In situ diagnosis of the electrolyte solution in a laminate lithium ion battery by using ultrafine multi-probe Raman spectroscopy. *J Power Sources* 359: 435–440.
200. Yamanaka T, Nakagawa H, Tsubouchi S, et al. (2017) In situ Raman spectroscopic studies on concentration change of electrolyte salt in a lithium ion model battery with closely faced graphite composite and $LiCoO_2$ composite electrodes by using an ultrafine microprobe. *Electrochim Acta* 234: 93–98.
201. Yamanaka T, Nakagawa H, Tsubouchi S, et al. (2017) Effects of pored separator films at the anode and cathode sides on concentration changes of electrolyte salt in lithium ion batteries. *Jpn J Appl Phys* 56: 128002.
202. Naudin C, Bruneel JL, Chami M, et al. (2003) Characterization of the lithium surface by infrared and Raman spectroscopies. *J Power Sources* 124: 518–525.
203. Galloway TA, Cabo-Fernandez L, Aldous IM, et al. (2017) Shell isolated nanoparticles for enhanced Raman spectroscopy studies in lithium–oxygen cells. *Faraday Discuss* 205: 469–490.
204. Park Y, Kim Y, Kim SM, et al. (2017) Reaction at the electrolyte–electrode interface in a Li-ion battery studied by in situ Raman spectroscopy. *Bull Korean Chem Soc* 38: 511–513.
205. Yamanaka T, Nakagawa H, Tsubouchi S, et al. (2017) In situ Raman spectroscopic studies on concentration of electrolyte salt in lithium ion batteries by using ultrafine multifiber probes. *ChemSusChem* 10: 855–861.
206. Lewis IR, Griffiths PR (1996) Raman spectrometry with fiber-optic sampling. *Appl Spectrosc* 50: 12A–30A.
207. Yamanaka T, Nakagawa H, Ochida M, et al. (2016) Ultrafine fiber Raman probe with high spatial resolution and fluorescence noise reduction. *J Phys Chem C* 120: 2585–2591.

208. Yamanaka T, Nakagawa H, Tsubouchi S, et al. (2017) In situ Raman spectroscopic studies on concentration change of ions in the electrolyte solution in separator regions in a lithium ion battery by using multi-microprobes. *Electrochem Commun* 77: 32–35.
209. Yamanaka T, Nakagawa H, Tsubouchi S, et al. (2017) Modification of the solid electrolyte interphase by chronoamperometric pretreatment and its effect on the concentration change of electrolyte salt in lithium ion batteries studied by in situ microprobe Raman spectroscopy. *J Electrochem Soc* 164: A2355–A2359.

AIMS Press